



# IronArc a New Process for Pig Iron Production; a Numerical and Experimental Investigation Focusing on Mixing

***Kristofer Bölke***

Doctoral Thesis  
Stockholm 2020

KTH Royal Institute of Technology  
School of Industrial Engineering and Management  
Department of Material Science and Engineering  
Unit of Process  
SE-100 44 Stockholm  
Sweden

---

Akademisk avhandling som med tillstånd av Kungliga Tekniska Högskolan i Stockholm, framlägges för offentlig granskning för avläggande av teknologie doktorsexamen, torsdagen den 7 maj 2020, kl 10.00 i Kollegiesalen, Brinellvägen 8, Kungliga Tekniska Högskolan, Stockholm.

---

ISBN 978-91-7873-481-8

Kristofer Bölke:

*An Experimental and Numerical Study to  
Investigate Important Mixing Phenomena  
in the New IronArc Process*

KTH School of Industrial Engineering and Management  
Unit of Process  
Royal Institute of Technology  
SE-100 44 Stockholm  
Sweden

ISBN 978-91-7873-481-8  
TRITA-ITM-AVL 2020:20

Copyright © Kristofer Bölke, 2020  
Print: Universitetsservice US-AB, Stockholm 2020

*“Process metallurgy is described sometimes as a science and sometimes as an art, but really it’s a battleground”*

- *Kristofer Bölke (inspired by Bill Bryson)*



# Abstract

---

The purpose of this study was to investigate and explore the mixing and related phenomena in the newly developed IronArc process, which uses submerged gas injection through plasma generators to melt and reduce iron oxide into pig iron. Specifically, the penetration depth and mixing times were investigated under different conditions due to their importance to the process. This was done both experimentally and through Computational Fluid Dynamics (CFD).

Firstly, a 1:3 scale acrylic plastic model of the pilot plant was developed, and both the penetration depth and mixing time were studied and determined for various conditions through physical experiments. Then, a mathematical model was created where an approach to predict the penetration depth numerically was validated for an air-water system. By using the validated model, the penetration depth in the pilot plant was predicted. Furthermore, a new method for determining the mixing time in a slag-based process was developed and used to determine the mixing time experimentally in the pilot plant with slag as liquid. Also, a slag investigation was made both by Thermo-Calc calculations and Light optic Microscope (LOM) observations to investigate the slag phase during real process conditions. Moreover, a numerical model was developed that predicted the mixing time for the small-scale model with air and water. The same CFD approach was then applied on the pilot plant in order to determine the mixing time. Finally, some experiments were also performed in the pilot plant in order to study the mixing time in a larger scale vessel. In this case the plasma generator was only used to inject air so that the mixing in the water filled reactor could be studied, there was no heating of the gas since that would have vaporized the water very quickly.

The average mixing times in the 1:3 scaled physical acrylic plastic model was determined to 7.6 s and 10.2 s respectively for a 95% and a 99% homogenization degree. This was achieved when one inlet and a flow rate of 282 NLmin<sup>-1</sup> was used. An increase by 15.8% and a 17.6% of the mixing time for the 95% and 99% degrees of homogenizations, when multiple gas inlets were used compared to only using one gas inlet. The penetration depth showed a pulsating behavior with a maximum and minimum value.

The penetration depth of the experimental air water system could be described accurately by the CFD model, where the results of the Euler-Euler approach corresponded to the experiments within 86%. It was also shown to reduce the computational time compared to the other tested Volume of Fluid (VOF) model approach. The penetration depth in the IronArc pilot plant was predicted to approximately 0.3 m, which was the same length as the radius of the reactor.

The overall results show that it was possible to experimentally determine the mixing time in the pilot plant by adding a tracer ( $\text{MnO}_2$  powder) to the slag. More specifically the time to homogenize the bath was reached in less than 10 seconds after the tracer addition. Both the LOM observations and Thermo-Calc calculations indicated that it was reasonable to assume that the slag was in a liquid state during process conditions at the operating temperature of the process.

The predicted mixing time for the numerical model was 7.5 seconds for the air-water system, which corresponds to a 1.3% difference compared to the experimental mixing times. The predicted mixing time was 6.5 seconds in the pilot scale simulations. In addition, these results are in line with the mixing time results determined through industrial trials which showed that the mixing times were less than 10 seconds. Similarly, the mixing time for the water-filled pilot plant was 8.5 seconds for a 95% degree of homogenization and 14 seconds for a 99% degree of homogenization.

This investigation of the novel IronArc process has produced valuable information on the mixing behavior that can be used in design decisions for at future large-scale ironmaking process.

**Keywords: Mixing time, Penetration depth, CFD simulations, IronArc, Water modeling, Mixing time Experiments**

# Sammanfattning

---

I den här studien så var syftet att undersöka omrörningen och relaterade fenomen i den nyutvecklade IronArc processen. Processen använder sig av gasinjektion genom plasmageneratorer för att smälta och reducera en slagg bestående av järnoxid. Både penetrationsdjupet hos gasen och omrörningstiden undersöktes under olika förhållanden för att de är viktiga parametrar för processen. Undersökningen har gjorts både genom experiment och Computational Fluid Dynamics (CFD).

Först utvecklades en nerskalad modell i akrylplast av IronArc pilot reaktorn i skala 1:3, där både penetrationsdjupet och omrörningstiden bestämdes för ett system med luft och vatten genom fysiska experiment. Sedan så skapades en matematisk modell för att beskriva penetrationen av luft injicerat i vatten. Den validerade modellen användes sedan för att beskriva penetrationsdjupet av den injicerade gasen i slaggen för pilotreaktorn. Vidare så utvecklades en ny metod för att bestämma omrörningstiden i pilotreaktorn med slagg som flytande medium. Slaggen undersöktes också både med hjälp av ljusoptiskt mikroskop (LOM) och även genom beräkningar i Thermo-Calc. Detta gjordes för att undersöka huruvida slaggen är i smält tillstånd då processen körs. Ytterligare en matematisk modell utvecklades sedan för att beskriva omrörningen i den nedskalade modellen av akrylplast med luft och vatten. Samma CFD modell användes för att beskriva omrörningen i pilotreaktorn, där modellen validerades mot de tidigare resultaten från de fysiska experimenten med slagg i pilotreaktorn. Slutligen så utfördes ytterligare försök i pilotreaktorn för att bestämma omrörningstiden, men med vatten istället för slagg. Det bör även nämnas att det enbart var luft som injicerades utan att gasen värmdes upp i plasmageneratoren, då vattnet skulle evaporerat om man värmt gasen.

Den genomsnittliga omrörningstiden för den nerskalade modellen där luft injicerades i vatten bestämdes till 7,6 s och 10,2 sekunder för respektive homogeniseringsgrad på 95% och 99%. Detta gjorde då ett inlopp användes med ett gasflöde på 282 NLmin<sup>-1</sup> användes. Det visade sig att den genomsnittliga omrörningstiden ökade med 15,8% för 95% homogenisering och 17,6% för 99% homogeniseringsgrad då 3 inlopp användes för samma gasflöde. Penetrationsdjupet visade på ett pulserande beteende med ett maximum och minimum värde för respektive undersökt gasflöde.

Penetrationsdjupet för experimentet med gas injicerat i vatten kunde beskrivas korrekt med CFD modellen, där Euler-Euler metoden bestämde

penetrationsdjupet av experimentet inom en noggrannhet på 86%. Det visade sig också att denna metod reducerade beräkningstiden jämfört med den andra testade Volume of Fluid (VOF) modellen. Penetrationsdjupet av gas i slagg predikterades till 0.3 m, vilket motsvarar radiens längd i reaktorn. Resultaten visade att möjligt att experimentellt bestämma omrörningstiden i pilotreaktorn genom att addera ett spårämne ( $\text{MnO}_2$  pulver) till slaggen och ta kontinuerliga prover. Mer specifikt så var tiden för att homogenisera badet under 10 sekunder efter att spårämnet tillsatts. Både LOM (Ljusoptiskt Mikroskop) observationerna och Thermo-Calc beräkningarna indikerade att det var rimligt att anta att slaggen är i smält tillstånd under körning.

Den predikterade omrörningstiden för den numeriska modellen för luft-vatten systemet var 7,5 sekunder och överensstämmer med experimentresultaten med 1,3%. omrörningstiden bestämdes till 6.5 sekunder för simuleringen av pilotreaktorn och det stämmer överens med resultaten från experimenten i pilotskalan som visade att omrörningstiden var under 10 sekunder. Även resultaten från experimenten då omrörningstiden bestämdes 8,5 och 14 sekunder för 95 % och 99% homogeniseringsgrad, då reaktorn var vattenfylld.

Denna undersökning av den nya IronArc-processen har gett värdefull information om omrörningen som kan användas i designbeslut för en framtida storskalig järnframställningsprocess.

**Nyckelord: Omrörningstid, Penetrationsdjup, CFD simuleringar, IronArc, Vattenmodellering, Omrörningsexperiment**



# Acknowledgement

---

First and foremost, I would like to express my sincere gratitude to both my supervisors at KTH Royal Institute of Technology, Associate Professor Mikael Ersson and Professor Pär Jönsson for all their guidance, valuable advice, fruitful discussions, support and positive encouragement throughout the project timeline. Also, I would like to thank my colleagues and the entire department of Material Science and Engineering at KTH for making this a very inspiring and fun journey with many laughs and good helpful discussions.

I would also like to thank the people at ScanArc, especially Maria Swartling and Matej Imris, for a good collaboration during this entire project.

A special thanks to *Swedish Energy Agency (Energimyndigheten)* for the financial support to be able to conduct the research presented in this thesis. Also, *Jernkontoret*, *Axel Hultgrens foundation* and *Yngströms foundation* for scholarships that made it possible to finish the final parts of it, as well as visiting scientific conferences.

Furthermore, I would like to thank my colleagues and my current employer, Linde Gas AB, for supporting me in finishing this thesis.

At last I would like to thank my friends and family. Especially, my parents Lottie and Pierre, my brother Alexander and my girlfriend Manda for their love and support, it means everything.



**Kristofer Bölke**

Stockholm, May 2020



# Supplements

---

The following supplements have been the basis for the thesis:

- Supplement 1:** “Physical Modeling Study on the Mixing in the New IronArc Process”, Kristofer BÖLKE, Mikael ERSSON, Peiyuan NI, Maria SWARTLING and Pär G. JÖNSSON, *Steel Research International*, 2018, Vol. 89, pp. 1-10.
- Supplement 2:** “Importance of the Penetration Depth and Mixing in the IRONARC Process”, Kristofer BÖLKE, Mikael ERSSON, Matej IMRIS and Pär JÖNSSON, *ISIJ International*, 2018, Vol. 58, pp. 1210-1217.
- Supplement 3:** “Experimental Determinations of Mixing Times in the IronArc Pilot Plant Process”, Kristofer BÖLKE, Mikael ERSSON, Nils Å. I. ANDERSSON, Matej IMRIS and Pär JÖNSSON, *Metals*, 2019, Vol. 9, pp. 1-15.
- Supplement 4:** “Physical and Numerical Modeling of the Mixing Time in the IronArc Pilot Plant”, Kristofer BÖLKE, Mikael ERSSON and Pär JÖNSSON, *Manuscript*.
- Supplement 5:** “Experimental study of the Mixing Time in the IronArc Pilot Plant Reactor”, Kristofer BÖLKE, Mikael ERSSON and Pär JÖNSSON, *Manuscript*.

The contributions by the author of this thesis to the above supplement are the following:

**Supplement 1:** Performed all of the literature survey, all of the experimental work, major part of analyses and major part of writing.

**Supplement 2:** Performed all of the literature survey, most part of the numerical work including the observations and analyses the numerical predictions and major part of writing.

***Supplement 3:*** Performed all of the literature survey, a big part of the experimental work, observations and analyses of the LOM work, Thermo-Calc calculations and major part of writing.

***Supplement 4:*** Performed all of the literature survey, major part of numerical calculation work and major part of writing.

***Supplement 5:*** Performed all of the literature survey, a big part of the experimental work and major part of writing.

# List of Tables

---

- Table 1. Overview of the 5 supplements
- Table 2. Parameters used in the physical water model experiments and in the real process.
- Table 3. Setup for industrial mixing time test by conductivity measurements
- Table 4. Shows the standard deviation, average value and the standard error of the samples with 1 minute interval, for trial 1 and trial 2.
- Table 5. Shows the initial amount of MnO, the added amount of MnO<sub>2</sub>, the total amount of MnO and theoretical amount of MnO in the slag, for the two trials performed.
- Table 6. Normalized slag composition for the different trials. The number of elements in the slag is also shown, since not all these composition values were not included in the table due to the low amount per element. Nr stands for the number of elements.
- Table 7. Penetration depths for the two multiphase models and for one experimental value.
- Table 8. overview of the supplements and the objective, approach, parameters and results



# List of Figures

---

- **Figure 1.** A schematic figure of the IronArc pilot plant process.
- **Figure 2.** Schematic figure of the future IronArc industrial scale process
- **Figure 3.** Layout of the 5 supplements and their connections.
- **Figure 4** Dimensions of the acrylic plastic model used in the water model experiments for determinations of the penetration depths and mixing times.
- **Figure 5.** A schematic figure of the experimental setup used for the physical model experiments.
- **Figure 6.** a) Position of conductivity probes in the water in the bottom part of the acrylic plastic model. b) The setup with three gas inlets seen from above.
- **Figure 7.** Schematic picture of the sampling procedure with addition of tracer and sampling rod.
- **Figure 8.** Position of conductivity probes in the IronArc pilot plant reactor.
- **Figure 9.** Experimental setup for the conductivity measurements performed in the IronArc pilot plant reactor
- **Figure 10.** Geometry of the water model domain.
- **Figure 11.** Medium mesh at a cross section plane of the domain.
- **Figure 12.** Numerical domain of the IronArc pilot plant simulation.
- **Figure 13.** Measured mixing times for a flow rate of  $282 \text{ NLmin}^{-1}$  for both a 95% and a 99% degree of tracer homogenization. Data are given for 6 trials.
- **Figure 14.** Data of normalized conductivity curves for two probes. These measurements were taken from the third trial when using one gas inlet. a) Shows the normalized conductivity values from 0 to 1.6. b) Shows the normalized conductivity values from 0.9 to 1.1. Horizontal lines that shows the areas for 95% and 99% degrees of homogenization are also shown.
- **Figure 15.** a) Mixing times for experiments using different flow rates when using one gas inlet. b) Mixing times for experiments using three gas inlets and the same flowrate. Data are presented for both 95% and 99% homogenization degrees.
- **Figure 16.** The measured air plume in the water for all tested flowrates.

- **Figure 17.** Penetration depths determined both experimentally and using the empiric equation at different flow rates. The experimental lines show the max and min values at each flow rate.
- **Figure 18.** The penetration of the air in the water for a flowrate of 400 NLmin<sup>-1</sup>. Data are presented for the minimum penetration (upper figure) and the maximum penetration (lower figure).
- **Figure 19.** Content MnO (%) for the different samples for trial 1 and trial 2, respectively. The MnO<sub>2</sub> powder was added after sample 2 for trial 1 and after sample 15 for trial 2.
- **Figure 20.** MnO (%) content for all the sample taken during the sampling for trial 3, where samples 1 and 2 are taken before a tracer addition and the rest of the samples are taken after an addition of the MnO<sub>2</sub> tracer powder.
- **Figure 21.** MnO (%) content for all the sample taken during sampling in trial 4, where samples 1 and 2 are taken before a tracer addition and the rest of the samples are taken after a tracer addition.
- **Figure 22.** The amount of % MnO in each slag sample taken during the pilot plant experiment.
- **Figure 23.** LOM picture of 2D cross section surface of slag sample. The numbers represent different zones in the sample.
- **Figure 24.** A piece of solidified slag from a macro perspective.
- **Figure 25.** The mass fraction of liquid phase for the slags used in trials 1 and 2 for a temperature span between 1000 and 2000 °C. The calculations were made for a closed system.
- **Figure 26.** The mass fraction of liquid phase in the slags used in trials 1 and 2 for a temperature span between 1000 and 2000 °C. The calculations were done by assuming an open system with an oxygen potential of 0.3
- **Figure 27.** The mass fraction of liquid phase in the slags used in trials 1 and 2 for a temperature span between 1000 and 2000 °C. The calculations were done by assuming an open system with an oxygen potential of 0.8.
- **Figure 28.** Normalized conductivity values for the two measurement probes. Inside the horizontal lines at 1.05 and 0.95 represents the area where the concentration of the tracer is within a 95% degree of homogenization.
- **Figure 29.** Isosurface of the air plume in water for the EE-simulation.



- **Figure 30. Isosurface of air plume in the water for the VOF-simulation.**
- **Figure 31. Volume fraction of air as a function of distance along the nozzle centerline for EE-simulation.**
- **Figure 32. Volume fraction of air as a function of distance along the nozzle centerline for VOF-simulation.**
- **Figure 33. Volume fraction of air when using the EE-model. Data are given for an yz-plane located in the center of the domain.**
- **Figure 34. Volume fraction of air when using the VOF-model. Data are given for an yz-plane located in the center of the domain.**
- **Figure 35. Volume fraction of gas for the pilot scale-model in an yz-plane located in the center of the domain**
- **Figure 36. Tracer concentration curves as a function of time for both predictions a) and b) and experiments c) and d)**
- **Figure 37. Tracer concentration curves for the pilot plant slag simulation.**
- **Figure 38. The shear stress on the wall of the pilot plant with the maximum shear stress of 30 Pa. It is shown from a) above, b) below, c) right side, d) left side, e) opposite side of the nozzle locations, and f) nozzle wall.**



# List of Symbols

---

$N_{Fr'}$	– Modified Froude number
$\rho_g$	– Density of gas
$\rho_l$	– Density of liquid
$d_0$	– Characteristic length of the system
$g$	– Gravitational acceleration constant
$u_0$	– Velocity of the gas at the inlet
$Q_m$	– Flowrate for model
$Q_R$	– Flowrate in real process
$\lambda$	– Scale factor
$H$	– Uniformity value, Concentration at a certain point in time over final concentration
$C(t)$	– Concentration at time $t$ of tracer in liquid bath
$C_f$	– Final concentration of tracer in liquid bath
$l_p$	– Penetration depth of gas injected into liquid
$t_{mixing}$	– Mixing time for both probes calculated as average value
$t_{p1}$	– Time for probe 1 to reach the homogenization degree
$t_{p2}$	– Time for probe 2 to reach the homogenization degree
$\alpha$	– Scalar quantity that describes the volume fraction of a phase
$\nabla$	– Nabla operator (vector differential operator)
$v$	– Velocity
$F$	– External forces acting on the object
$p$	– Pressure
$\partial$	– Partial derivative
$\mu_g$	– Viscosity for gas phase
$\mu_l$	– Viscosity for liquid phase
$\dot{m}_{pq}$	– Mass transfer from $p^{th}$ phase to the $q^{th}$ phase
$\bar{\tau}$	– Stress strain tensor
$F_q$	– External body force between the phases
$K_{pq}$	– Exchange coefficient between the phases
$\tau_p$	– Particular relaxation time
$f$	– Drag function
$A_i$	– Interfacial area
$C_D$	– Drag coefficient
$Re$	– Reynolds number
$\mu_t$	– Turbulent viscosity

$k$	– Turbulent kinetic energy
$\varepsilon$	– Rate of dissipation of turbulent kinetic energy
$u_j$	– Velocity component in corresponding direction
$G_k$	– Production of turbulent kinetic energy due to mean velocity gradient
$G_b$	– Production of turbulence kinetic energy due to bouancy
$\sigma_k$	– Prandts constant for the turbulent kinetic energy (=1.0)
$\sigma_\varepsilon$	– Prandts constant for the dissipation rate of turbulent kinetic energy (=1.2)
$Y_M$	– The contribution of the fluctuating dilatation in compressible turbulence to the overall dissipation rate
$S_k$	– User define source term for the turbulent kinetic energy
$C_1$	– Coefficient in the realizable model
$S_\varepsilon$	– User define source term for the dissipation rate of turbulent kinetic energy
$C_{3\varepsilon}$	– Constant in the realizable turbulent model
$C_2$	– Constant in the realizable turbulent model (=1.9)
$C_{1\varepsilon}$	– Constant in the realizable turbulent model (=1.44)
$Y$	– Mass fraction of species
$J$	– Diffusion flux of species
$SC_t$	– Turbulent Schmidt number
$D_m$	– Mass diffusion coefficient
$C_\mu$	– Constant for the turbulent viscosity

# List of Abbreviations

---

AOD process	– Argon oxygen decarburization process
C	– Carbon
CO	– Carbon monoxide
CO <sub>2</sub>	– Carbon dioxide
CFD	– Computational fluid dynamics
CaO	– Calcium oxide
EE	– Euler-Euler, Eulerian multiphase model
Fe <sub>3</sub> O <sub>4</sub>	– Magnetite
Fe <sub>2</sub> O <sub>3</sub>	– Hematite
FeO	– Wustite
Fe	– Iron
H <sub>2</sub>	– Hydrogen
H <sub>2</sub> O	– Water
LPG	– Liquefied petroleum gas
LOM	– Light optical microscope
MnO <sub>2</sub>	– Manganese dioxide
MnO	– Manganese oxide
MgO	– Magnesium oxide or magnesia
NiO	– Nickel oxide
NaCl	– Natrium chloride
Pa	– Pascal
PG	– Plasma generator
VOF	– Volume of fluid
Wt%	– Weight percent
NLmin <sup>-1</sup>	– Normal liter per minute
Nm <sup>3</sup> h <sup>-1</sup>	– Normal cubic meter per hour
XRF	– X-ray fluorescence spectrometry
TCOX7	– Database in Thermo-Calc
PISO	– Pressure-implicit with splitting of operators
PD	– Penetration depth
STD	– Standard deviation
SiO <sub>2</sub>	– Silicon dioxide
Al <sub>2</sub> O <sub>3</sub>	– Aluminum oxide



# CONTENTS

---

Abstract .....	i
Sammanfattning .....	iii
Acknowledgement .....	v
Supplements .....	vii
List of Tables .....	ix
List of Figures .....	xi
List of Symbols .....	xv
List of Abbreviations .....	xvii
1. INTRODUCTION .....	1
1.1. BACKGROUND .....	1
1.2. PRESENT WORK .....	5
1.3. OBJECTIVES OF THE WORK .....	8
2. METHODOLOGY .....	11
2.1. EXPERIMENTAL METHODS .....	11
2.1.1 SMALL SCALE PHYSICAL MODELING .....	11
2.1.2. INDUSTRIAL PILOT PLANT TRIALS .....	16
2.2. NUMERICAL MODEL .....	20
2.2.1 ASSUMPTIONS .....	20
2.2.2 MULTIPHASE THEORY .....	21
2.2.3 BOUNDARY CONDITIONS AND SOLUTION METHODS .....	25
3. RESULTS AND DISCUSSION .....	29
3.1. EXPERIMENTAL PART .....	29
3.1.1 SMALL SCALE WATER MODELING (SUPPLEMENT 1) .....	29
3.1.2 PILOT PLANT TRIALS (SUPPLEMENTS 3 & 5) .....	35
3.2. NUMERICAL MODELING (SUPPLEMENTS 2 & 4) .....	46

3.2.1 PENETRATION DEPTH (SUPPLEMENT 2) .....	46
3.2.2. MIXING TIME.....	53
4. CONCLUDING DISCUSSION .....	57
5. CONCLUSIONS .....	61
6. SUSTAINABILITY & FUTURE WORK .....	65
6.1 SUSTAINABILITY .....	65
6.2 RECOMMENDATIONS OF FUTURE WORK.....	65
7. REFERENCES .....	67



# 1. INTRODUCTION

---

## 1. 1. BACKGROUND

Today, the blast furnace process is the most widely used process to reduce iron ore and to produce pig iron. In the steel industry, the iron ore based production is a large source of CO<sub>2</sub> emissions, since almost all of the iron reduction processes are coal based.[1, 2] Worldwide, the CO<sub>2</sub> emissions in the iron and steel industry stands for approximately 4% to 7% of the total world CO<sub>2</sub> emissions.[3] According to another source, the World steel association, that number is 6.7%.[4] In addition to the large amounts of emissions from the iron and steel industry, it is also one of the industries that consumes the largest amount of energy among manufacturing industries. Therefore, a lot of research has been made in order to reach a more energy efficient production of pig iron.[1-9] Also, in order to control the blast furnace process more efficiently and to get a more stable process.[10] As a result of all efforts, the pig iron production in the blast furnace have become more efficient. However, since the blast furnace still uses coke as the main energy source it is difficult to reach further reductions with respect to the CO<sub>2</sub> emissions.[5]

Due to the emissions and large energy consumption during the production of pig iron in the blast furnace, the development of new technologies are of interest. IronArc is a future new emerging process for pig iron production through reduction of iron oxide and preliminary calculations have shown that it will reduce both CO<sub>2</sub> emissions and energy usage compared to existing technologies.[11]

Currently, this process exists in a pilot scale, as seen in Figure 1. [11] In this process, hematite and magnetite are charged into the cylindrically shaped reactor. This material is melted, and a slag is created, when a hot carrier gas is injected through a plasma generator. The plasma generator (PG) heats the gas mixture of air and LPG (Liquefied Petroleum Gas) to a very high temperature, which is approximately 20000°C in the PG. Thereafter, it is injected into the slag with a temperature of 3500 - 4000°C. The temperature drop of the injected gas is fast when it leaves the PG. A CO gas is created when the LPG is heated together with air and is used as a reductant in the reduction step where hematite and magnetite is reduced to wüstite. H<sub>2</sub> is also created when the LPG is heated and reduces the hematite and magnetite to wüstite, as well. Then, carbon is used as

reductant for the final reduction step where wüstite is reduced to pig iron. The reaction steps for this process can be seen in equations (1) – (5).

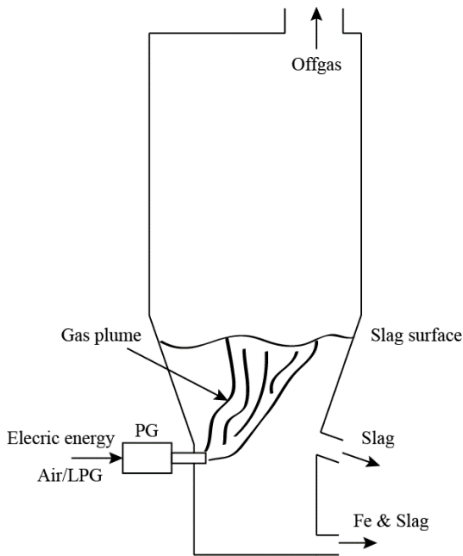
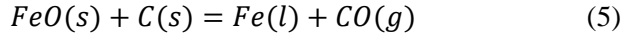
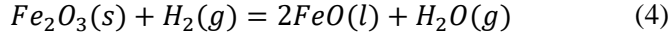
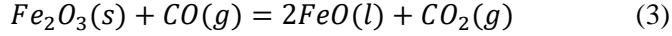
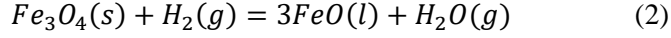
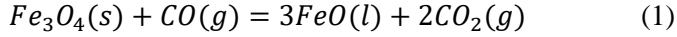


**Figure 1: A schematic figure of the IronArc pilot plant process.**

For the existing IronArc pilot plant all the reduction appears in one reactor, but for the future industrial plant the idea is that the reduction step will appear in two reactors. A schematic picture of an example of the future industrial scale can be seen in Figure 2. The hematite and magnetite are reduced completely by the injected gas from the PG in the first reactor and then the wüstite is transported through a channel to the second reactor. The final reduction is done by additions of carbon. The off gas from the second

reactor is cleaned, cooled and recirculated as a reducing agent which is used in the first reactor. [11]

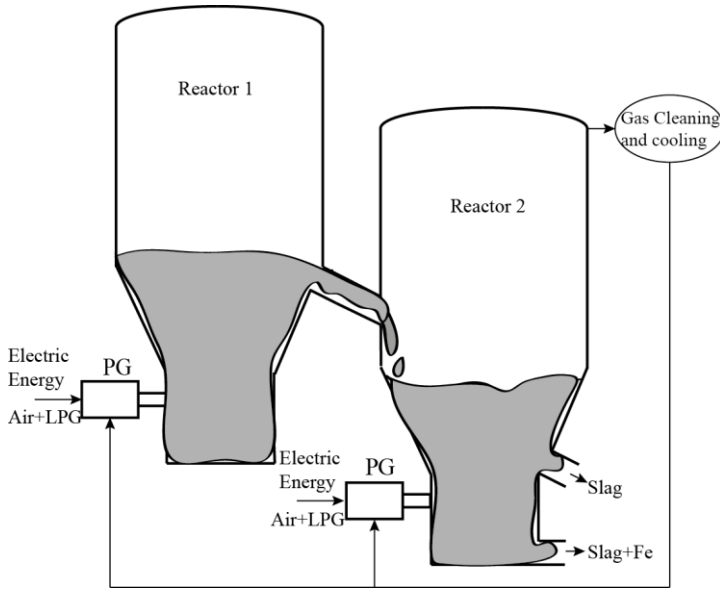


**Figure 2: Schematic figure of the future IronArc industrial scale process.**

Detailed information about the stirring and fluid flow is of great interest for the current process development. Especially, since the injected gas is used for heating, stirring and reduction. During injection from the horizontally placed nozzle submerged under the bath, the gas will penetrate a certain distance into the bath (penetration depth) before rising upwards in a swarm of bubbles due to buoyancy forces. This will create both stirring and mixing in the bath. [12] Therefore, both the mixing time and penetration depth are of great importance in this new emerging process and plays a big part for a future upscaling to a future industrial scale.

Since this is a new process, there are not much information in the open literature. However, there are several other metallurgical processes which use gas injection. [13-15] Both the mixing and stirring as well as the penetration depth is important parameters for these processes. Often, small-scaled (usually scaled between 1:3 to 1:10) physical models with air injection into water are used to simulate different metallurgical processes. [16-33] To maintain a dynamic similarity between model and real process, the modified Froude number is used to a large extent when scaling the models.[16-19, 21-29, 31-33] Both the penetration depth [18,

24, 28-30, 33] and the mixing time [16-22, 25, 27-30, 32] is frequently investigated parameters for small scaled physical water modeling experiments. For the mixing time experiments conductivity measurements are often used to determine the mixing time. [16-18, 22, 25, 27, 28, 30, 32]. Many examples are found that uses side blowing of air into water. [5-33] In some of these cases both top and side blown reactors are investigated. [18, 26, 30, 32]. In rarer cases all three of top, bottom and side blown converters have been investigated.[18]

It has been shown earlier that the penetration depth depends on several different factors. Firstly, the penetration depth increases with an increased gas flow rate, an increased modified Froude number and an increased ratio of gas density over liquid density. [34] Different phenomenon occurs during gas injection into a liquid bath, some at different stages or at different length scales. When observing the gas injection near the nozzle there are phenomenon like creation of bubbles, coalescence of bubbles and bubble break ups. [35] Moreover, the penetration depth is more dependent on the gas flow rate than the bath depth. [36]. Furthermore, the movement of the injected gas in a liquid will cause the surrounding liquid to move such that a flow is created in the liquid bath [37]. The resulted flow is turbulent, which results in good mixing conditions between the gas and liquid phases with a fast mass transfer rate between these. The transition of the gas jet into a swarm of bubbles gives a large contact area between the gas and liquid phases [38]. A too short penetration depth will result in refractory wear on the nozzle wall and a reduced mixing due to that the bubbles are not distributed in the entire bath. [34] A smaller diameter of the inlet and in turn higher injection velocity have been shown to increase the penetration depth. [29]

Similarly, it has been shown that the mixing time is dependent on several factors, such as the gas flow rate and converter diameter. An increase in gas flow rate decreases the mixing time, due to a more powerful stirring of the bath. Moreover, an increased diameter results in an increased mixing time. [19] [22] It is a little bit unclear how the bath depth affects the mixing time. It seems that when side blowing is used, the effect of bath depth is negligible. [19] However, for a bottom blown process, the bath depth seems to have a greater impact on the mixing time. A greater bath depth seems to result in an increased mixing time, and vice versa. The positioning of the bottom injection tuyeres affects the mixing time as well. [39] Also, the mixing time have been shown to be dependent on the position of the tracer addition. The mixing time increases when the tracer is added closer to the surface.[19] In a study, side blowing was introduced to a top and bottom blown converter and decreased the mixing time in the bath. [18]

When a swirling motion is induced to the bath a strong mixing is expected due to this swirling flow. [40]

Another effective tool for investigating mixing and gas injection is numerical modeling or CFD modeling. With CFD modeling many process parameters can be predicted and useful knowledge can be gained, which would be difficult to achieve otherwise. The Penetration depth is one example, since it is difficult to measure in metallurgical converters due to the prevailing conditions, knowledge regarding the gas injection and penetration depth can be obtained through CFD calculations. This has been done successfully multiple times earlier. [16, 18, 29, 41-46] Both for side-blown [29, 41, 42, 46] and top blown [16, 43, 44] processes. VOF (Volume of Fluid) model is a popular model that is used for this purpose [29, 46, 18], but a Eulerian-Eulerian approach have been applied for this purpose as well.[42] Sometimes the criteria for the penetration depth have been defined the farthest depth an 80% volume fraction of the injected gas have reached. [42, 47]

The fluid dynamics, stirring and mixing time have been investigated and predicted frequently throughout the years by CFD calculations [16, 48-57]. Both by using an VOF setup for predicting the gas and liquid interface [55], by Euler-Euler approach [56] and Euler-Lagrange approach [48]. These numerical models have been compared with respect to simulations of a top blown ladle [57].

As described above physical small-scale modeling along with CFD modeling are often used to investigate phenomena's in these metallurgical processes. However, there are not many processes where the mixing time have been investigated in the full-scale industrial processes within the steel industry, especially when measuring the tracer content as a function of time. In some investigations radiotracers have been used to measure the efficiency of mixing in industries, such as; petrochemicals, oil and gas and wastewater plants. In these cases, the radiotracer is injected at the inlet and thereafter monitored at the outlet, which enables a determination of the mixing efficiency [58, 59].

## 1.2. PRESENT WORK

In this work the important fluid flow characteristics, penetration depth and mixing time, have been investigated in the IronArc pilot plant process. These parameters were investigated due to their importance to the process. The studies have been done by using small scale physical water modelling, pilot plant trials and CFD calculations. Furthermore, the slag phase properties were investigated both by using graphical LOM observations

and Thermo-Calc calculations. This thesis and work consist of 5 supplements. A layout of the thesis and the supplements can be seen in figure 3 and a short description of each supplement is seen below:

### ***Supplement 1***

In the first supplement small scale physical modelling experiments were performed in a 1:3 scale model of the IronArc pilot plant reactor. Both the penetration depth and mixing time were investigated under different conditions, with air and water as gas and liquid during the experiments. The mixing time was determined through conductivity measurements and the tuyere numbers effect on the mixing time were investigated, along with flow rate. Furthermore, the penetration of the injected gas was investigated for several flow rates and studied by both a high-speed camera as well as a film camera.

### ***Supplement 2***

The second supplement focused purely on numerical calculations in terms of CFD predictions. Firstly, two different approaches for multiphase flows were investigated and compared to results from physical water model experiments. This was done to validate the numerical model and determine which multiphase model that were suitable to use for this new IronArc process. Then, the validated numerical model was used to predict the penetration depth in the IronArc pilot plant.

### ***Supplement 3***

In the third supplement, industrial trials were performed, and the mixing time was determined in the IronArc pilot plant during real process conditions. A new experimental approach was applied where a powder of  $\text{MnO}_2$  was used as tracer, and continuous sampling was made. This was done for 5 trials. Then, the slag phases during operation were investigated through using both LOM-observations and Thermo-Calc calculations. Specifically, to determine the fraction of liquid phase.

### ***Supplement 4***

With input from both *supplement 1* and *supplement 3*, a numerical model was created that predicted the mixing time by CFD calculations according to the small-scale physical model. The results were validated against the 1:3 scale water model results. Then the same numerical approach was applied on the IronArc pilot plant, with input from the industrial trials performed such as slag phase properties and overall process parameters.

These mixing time results were also validated with the mixing time results obtained from the industrial experimental trials.

### ***Supplement 5***

During a reconstruction of the IronArc pilot plant, the opportunity was given to fill the reactor with water and perform mixing time experiments by conductivity measurements in the pilot plant. This was done in the fifth supplement and was done in a similar manner as the earlier conductivity measurements in the smaller model.

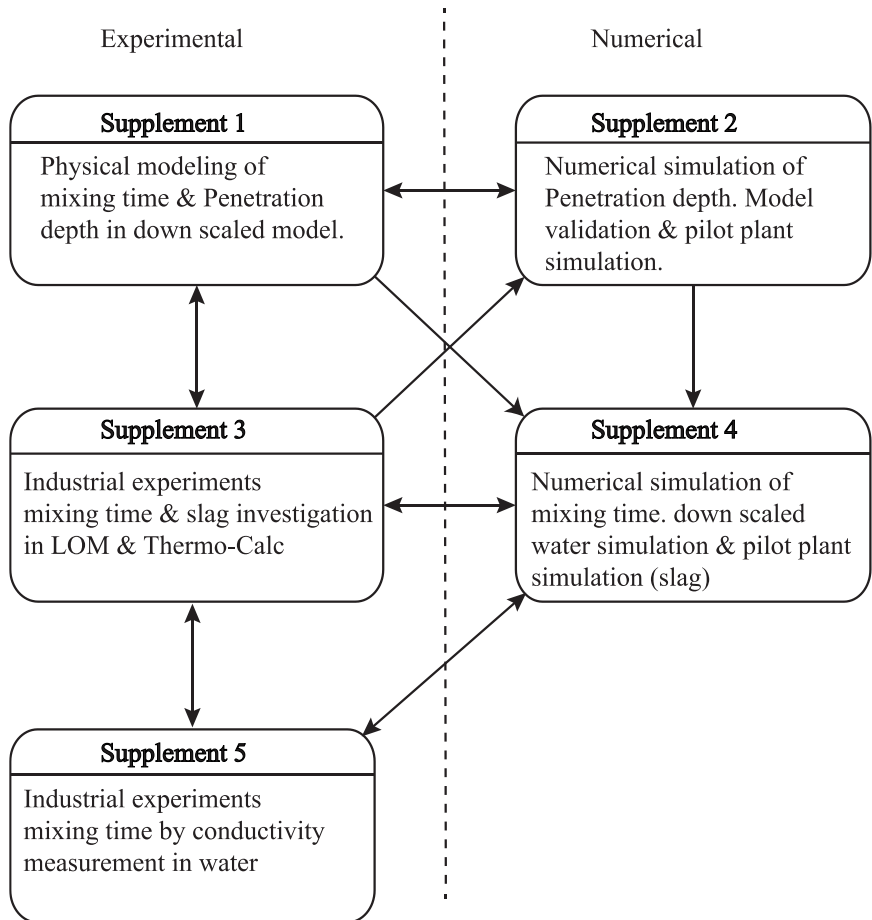


**Figure 3. Layout of the 5 supplements and their connections.**

### 1.3. OBJECTIVES OF THE WORK

The 5 supplements of this thesis were focused on the fluid behaviour and mixing of the IronArc pilot plant process during submerged injection of gas into the liquid bath of the process. Since this process depends on an efficient distribution of the gas in the slag and a fast homogenization of the slag, this thesis work focused on investigating both the penetration depth and mixing time of the IronArc pilot plant process. An overview of the 5 supplements can be seen in table 1. In *supplement 1* the objective was to determine the mixing time and investigate the penetration depth in a small-scale model. This was done in order to learn more about the mixing and behaviour of the bath during submerged gas injection and to obtain useful data that could be used as input data for the numerical modelling. Furthermore, in *supplement 2* the objectives were to find a suitable approach to determine the penetration depth by predicting the penetration depth for air injected into water. Then with a validated model determine the penetration depth in the IronArc pilot plant process. CFD is an efficient way to be able to predict and get an idea of the penetration depth since that parameter is extremely difficult to measure in the actual process. The penetration depth result is useful information for both the pilot plant process, but mainly that information is particularly interesting for the possible up scaling of the IronArc process. Moreover, in *supplement 3* the objectives were to determine the mixing time in the pilot plant process by experimental trials. Also, to investigate the liquid slag phases during operation. This was important when numerical calculations of the pilot plant were performed, since the amount of liquid phase affects the properties of the slag. The results were also important since it was used as validation for the numerical calculations and predictions of the mixing time in *supplement 4*. This were the objectives in *supplement 4* to predict the mixing time in the small scaled water model and validate the numerical approach, and then determine the mixing time in the IronArc pilot plant by CFD calculations and validate these results with the results from *supplement 3*. Finally, the objective of *supplement 5* was to determine the mixing time in the pilot plant but instead of slag, water was used as liquid. Finally, these results were compared to earlier experimental results.



**Table 1. Overview of the 5 supplements**

	<b>Study:</b>	<b>Objective:</b>	<b>Approach:</b>	<b>Parameters:</b>
<b>1</b>	Physical modeling study on the mixing in the new IronArc process	Investigate and determine the mixing time and penetration depth. Obtain data for numerical simulations.	Down scaled physical water modeling. Conductivity measurements for mixing time. Video recordings, camera photos and high-speed camera used for penetration depth.	Data from pilot plant and Industrial trials used when the 1:3 scale model setup was made.
<b>2</b>	Importance of the penetration depth and mixing in the IRONARC process	Compare suitable methods for determining penetration depth and validate the numerical model. Determine penetration depth in pilot plant.	Build up numerical model that corresponded to pilot plant. Compared VOF and Eulerian multiphase models in FLUENT for validation.	Data from Pilot plant and industrial trials.
<b>3</b>	Experimental determinations of mixing times in the IronArc pilot plant process	Determine the mixing time in the pilot plant experimentally. Determine slag phase during operation of process.	Addition of tracer in pilot plant and thereafter sampling during operation. LOM and Thermo-Calc investigation of the slag.	Data from pilot plant, LOM from slag sample and Thermo-Calc
<b>4</b>	Numerical investigation of the mixing time in the IronArc pilot plant	Validate a numerical model for mixing time from water modeling. Simulate mixing time in pilot plant process.	Numerical simulations of water model experiments as validation. Determine mixing time with validated model in pilot plant.	Data from the physical modeling experiments and from pilot plant and industrial trials.
<b>5</b>	Physical modeling of the mixing in the IronArc pilot plant reactor	Investigate the mixing time in the pilot plant when filled with water, with known parameters. As comparison to mixing time measurements in previous supplements.	Pilot plant partially filled with water and saline solution added with conductivity measurements to determine the mixing time.	Data from pilot plant and from down scaled acrylic plastic model (same approach for the experimental setup).



## 2. METHODOLOGY

---

This thesis includes both an experimental part and a mathematical modeling part. The experimental part includes small scale water modeling experiments (water and air as media), where both mixing times and penetration depths were determined (*Supplement 1*). Also, slag investigation (LOM and Thermo-Calc) and mixing time determinations pilot plant trials, with air and slag as liquid media, were also carried out (*Supplement 3*). In *supplement 5* the mixing time was determined in the pilot plant with the same approach as in supplement 1 (air and water), but in the pilot plant. The numerical part includes *supplement 2*, where a numerical model for the penetration depth is validated and the penetration depth of the pilot plant process is investigated. In *supplement 4*, the mixing time is predicted both for the water model as well as for the pilot plant process. The methodology for the experimental and numerical is described in the sections below (as well as in the separate supplements).

### 2.1. EXPERIMENTAL METHODS

#### 2.1.1 SMALL SCALE PHYSICAL MODELING

##### 2.1.1.1 MIXING TIME

The model of the pilot plant was made of acrylic plastic. Thus, all the lengths in the model are 1/3 of the corresponding pilot plant reactor lengths in order to maintain a geometric similarity between the model and the pilot plant reactor. The dimensions of the 1:3 scaled model can be seen in figure 4.

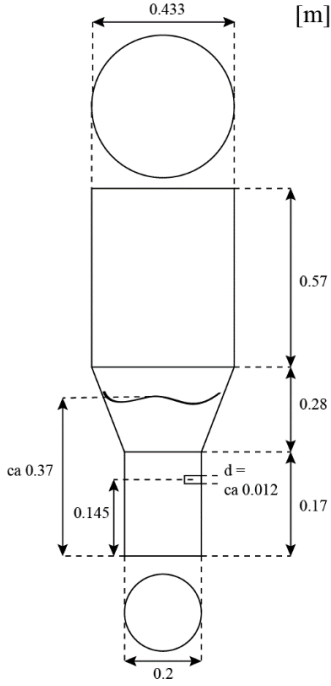


**Figure 4. Dimensions of the acrylic plastic model used in the water model experiments for determinations of the penetration depths and mixing times.**

The dynamic similarity between the model setup and the pilot plant setup was realized by using the modified Froude number. It is defined as the ratio of inertial forces to the buoyancy forces (equation 6):

$$N_{Fr'} = \frac{\rho_g u_0^2}{g \rho_l d_0} \quad (6)$$

where  $N_{Fr'}$  is the modified Froude number,  $\rho_g$  ( $\text{kgm}^{-3}$ ) and  $\rho_l$  ( $\text{kgm}^{-3}$ ) are the densities for the gas and the liquid, respectively. The parameter  $u_0$  ( $\text{ms}^{-1}$ ) is the velocity of the gas at the inlet,  $g$  ( $\text{ms}^{-2}$ ) is the gravitational acceleration constant, and  $d_0$  (m) is the characteristic length of the system. In this case, the characteristic length represents the diameter of the reactor. The flow rate was scaled based on equation (7). This equation is frequently used for scaling of flow rates when the modified Froude number is used as the similarity criteria. [21-29]

$$Q_m = Q_R \lambda^{2.5} \quad (7)$$

where  $Q_m$  ( $\text{m}^3\text{s}^{-1}$ ) is the flowrate for the downscaled model,  $Q_R$  ( $\text{m}^3\text{s}^{-1}$ ) is the flowrate in the real process, and  $\lambda$  is the scale factor with the value of 1/3 in this case. The diameter of the inlet was obtained from the following equation, when both the velocity and flow rate were given:

$$Q = \frac{u\pi d^2}{4} \quad (8)$$

The mixing time is defined as the time it takes to homogenize a liquid content in a tank or container, to a chosen degree of homogenization. Moreover, the mixing time, in this study was defined as the time for the bath to reach a homogenization degree of 95% of the final tracer concentration after a tracer solution had been added to the liquid bath. Specifically, for the uniformity value,  $H$ , to reach values between 0.95 and 1.05. In addition, the time to reach 99% homogenization degree in the bath was determined. Below, the definition of  $H$  can be seen in Equation (9):

$$H = \frac{C(t)}{C_f} \quad (9)$$

where  $H$  is the degree of homogenization,  $C(t)$  is the concentration at time  $t$  and  $C_f$  is the final concentration value in the water after a complete homogenization. The tracer concentration is measured and determined at two locations in the water bath. Sometimes, the mean value of the different measurement positions is applied to obtain the mixing time. [16-18] In the experiments, water and compressed air was used as the liquid and gas. The complete experimental set up can be seen in figure 5.

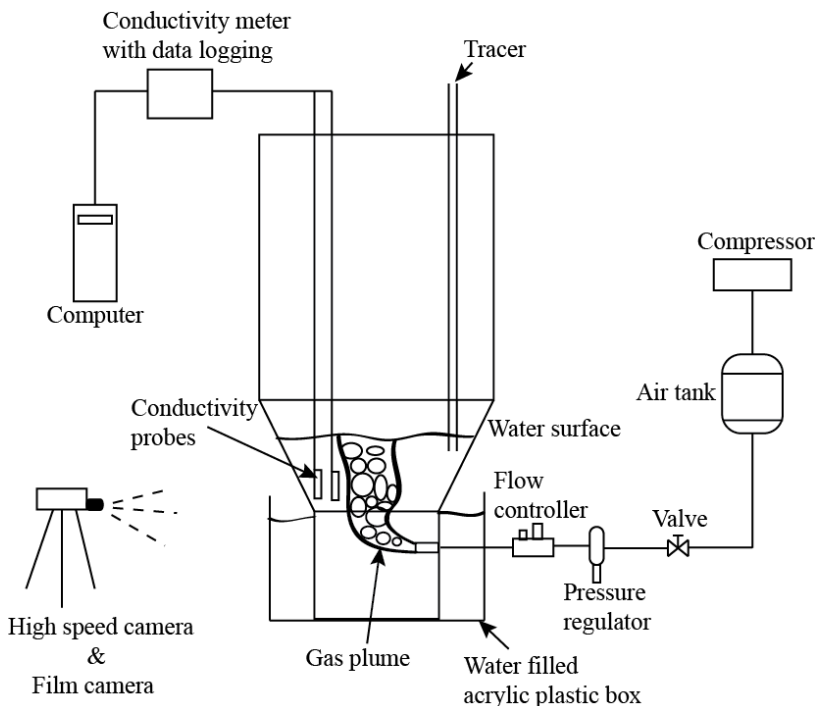


**Figure 5. A schematic figure of the experimental setup used for the physical model experiments.**

The compressed air was blown into the water through a nozzle that was fastened through the acrylic plastic wall. A flowmeter measured and controlled the air flow rate. At the beginning of the experiment, a tracer solution consisting of a 20wt% NaCl solution was added to the bath. Thereafter, the conductivity in the water was measured by using two conductivity probes, which were placed at different positions in the bath (Figure 6 a)). The probes used for conductivity measurements enabled a temperature compensation, meaning that the measured conductivity corresponds to a value at the reference temperature of 25 °C. The data obtained from the probes was logged every second during the entire time of the experiments. The time required for the probes to measure a concentration reaching a 95% homogenization degree of the final concentration in the liquid bath was determined as the mixing time. A sodium chloride solution (20wt %) tracer was added to the water when the flow field was fully developed (the blowing was done for a time that was several times longer than the mixing time for this process). The experimental parameters and conditions are given in table 2.

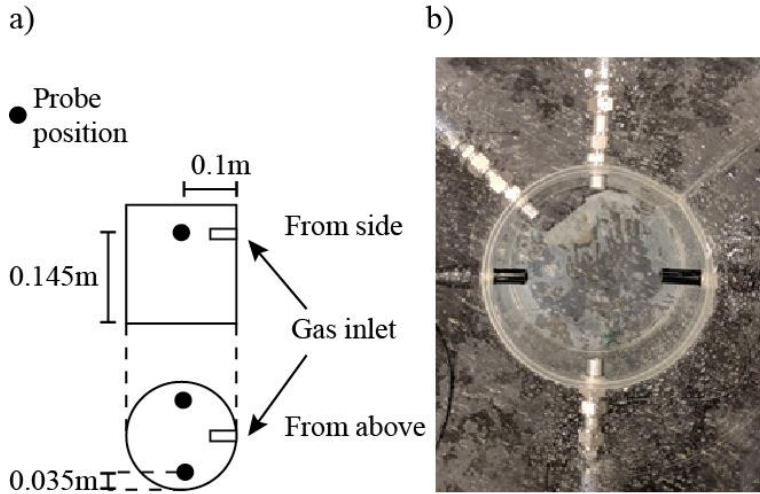


**Figure 6. a) Position of conductivity probes in the water in the bottom part of the acrylic plastic model. b) The setup with three gas inlets seen from above.**

**Table 2. Parameters used in the physical water model experiments and in the real process.**

Parameters	Physical model	Real process
Scale	1:3	1
Flow rate ( $\text{Nm}^3\text{h}^{-1}$ )	17	265
Bath depth liquid (m)	0.37	1.1
Nozzle height location (m)	0.145	0.435
Density liquid ( $\text{kgm}^{-3}$ )	998.2	3562
Density gas ( $\text{kgm}^{-3}$ )	1.226	0.1887
Diameter of lower cylinder (m)	0.2	0.6
Diameter of upper cylinder (m)	0.433	1.3
Diameter tuyere (m)	0.0117	0.035

### 2.1.1.2 PENETRATION DEPTH

The gas plume in the bath was studied by using a high-speed camera (MotionBlitz Cube 4), with the capability of capturing 1000 frames per second, and a film camera (Panasonic HDC-TM900). The Penetration depth (the depth of the injected gas at the tuyere level), was measured at several different flow rates by investigating both the pictures taken with the high-speed camera as well as the video from the film camera. The setup (seen in figure 5), were similar as for the mixing time experiments except for that no probes were present in the water. Also, a water filled acrylic plastic box were used to reduce reflections from the curved cylindrical shape of the water model. The penetration depth were determined for the following gas flow rates: 100, 200, 300, 400, 500 and 600 NLmin<sup>-1</sup>. The diameter of the tuyere inlet was 0.012 m and the bath height was also kept constant at a value of approximately 0.37 m, before the blowing through the submerged nozzle. The model and the gas plume in the water are illustrated in figure 1 b). The resulted penetration depths at the measured flow rates were compared with an empiric equation suggested by Oryall and Brimacombe.[34]:

$$l_p = 10.7 N_{Fr'}^{0.46} d_0 \left( \frac{\rho_g}{\rho_l} \right)^{0.35} \quad (10)$$

where  $l_p$  is the penetration depth,  $N_{Fr'}$ , is the modified froude number,  $d_0$  (m) is the diameter of the inlet,  $\rho_g$  and  $\rho_l$  (kgm<sup>-3</sup>) are the density of the gas and liquid, respectively. This relationship is frequently used in the literature. [29][37]

## 2.1.2. INDUSTRIAL PILOT PLANT TRIALS

### 2.1.2.1 MIXING TIME

#### 2.1.2.1.1 SLAG AS LIQUID MEDIA

The mixing time in the IronArc pilot plant process was investigated in plant trials by adding a tracer to a liquid slag and by measuring the tracer concentration over time, as it gets homogenized in the slag due to the stirring and mixing created by the injected gas through a submerged nozzle placed horizontally on the reactor wall. To do this, sampling (at the same depth) of the slag was made continuously by sampling rods. The time for each sample was measured from the moment the tracer was added. When the tracer concentration in the slag had reached its final value, the time for homogenization, i.e the mixing time, could be determined. Shortly described; in trials 1 and 2 for the pilot plants trials, the samples were taken



at one-minute intervals. In trials 3, 4 and 5 the samples were taken as fast as possible. Thereafter, XRF analysis was used to determine the tracer content in the samples after solidifying.

The tracer was added from an opening in the roof and the experiment was performed under oxidizing conditions, since the mixing time was of interest and not the yield of different elements in the process. A schematic figure of the sampling procedure can be seen in figure 7. It graphically shows how the tracer spreads in the slag over time and how continuous sampling was done throughout the trials.

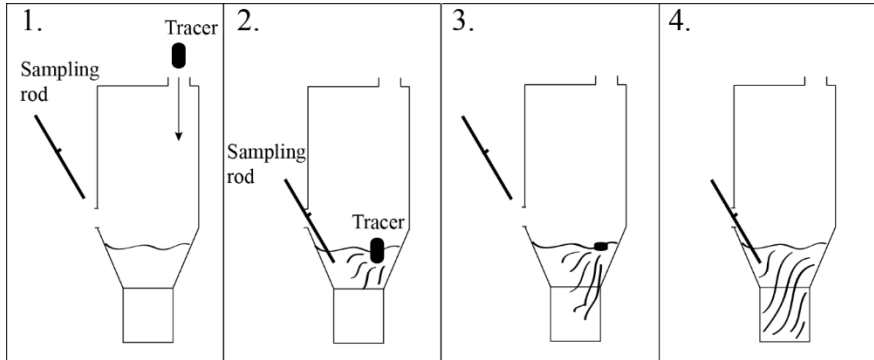


**Figure 7: Schematic picture of the sampling procedure with addition of tracer and sampling rod.**

The chosen tracer was a  $\text{MnO}_2$  powder with a size in the micrometer range. This was chosen due to the low content of MnO in the initial slag and also due to its low melting temperature. A low initial amount of MnO in the slag assures that the added  $\text{MnO}_2$  powder will appear in the XRF examination of the samples.  $\text{MnO}_2$  has a melting temperature of around  $535^\circ\text{C}$  [60] and it decomposes to other MnO-compounds at higher temperatures. This means that it will melt quickly at the operating temperature during addition and form  $\text{Mn}_3\text{O}_4$  or MnO depending on the available oxygen [60-61]. It was important that a tracer with low melting point was used, since a too high melting point of the tracer would result in too long dissolution times of the tracer in the slag bath. This would make it difficult to determine the mixing time since the time for mixing of the bath was of interest and not the time for dissolving the added powder.

#### 2.1.2.1.2 SLAG INVESTIGATION

A slag investigation was made to determine the slag characteristics. Namely, determining the phase during operation and the viscosity of the slag. Both these factors are important parameters for the numerical

calculations. Both light optic microscope (LOM) determinations and Thermo-calc software [62] calculations were done in order to investigate the slag.

Samples of the slag were taken and quenched in both water and air. The slag samples were investigated by using a LOM to examine the liquid and solid fractions in the slag. The microstructure of the samples was examined for particles that were not part of the cooling process. The presence of these types of particles in the slag would indicate that the particles existed before the cooling started and in that case they would most likely have been in a solid state in the slag. Therefore, the fraction of this kind of particles would represent the solid phase in the slag. This is important to investigate to determine the viscosity of the slag, since a liquid slag has a lower viscosity compared to a slag that is made up of two phases and which contains a significant number of solid particles. This information is of interest to determine the characteristics of the slag during operation, as well as for carrying out numerical modeling calculations of the process where the viscosity is an important parameter. The Thermo –Calc software [62] were also used to investigate the slag phases. Moreover, to calculate predictions of the liquid amount of the slag during the operational conditions as complement to the LOM investigation. The database TCOX7 were used and this database uses 18 elements and is intended for solid or liquid sulfides or oxides and used for slag calculations as well as for other applications [63]. These calculations were performed for all trials and for respective slag.

#### 2.1.2.1.3 WATER AS LIQUID MEDIA

This industrial test was performed in a similar way as for the conductivity experiments performed in the 1:3 scaled acrylic plastic model [64]. However, there were some small differences. Specifically, the probes were positioned at the same side (figure 8) and the tracers were added on the right-hand side of the nozzle. Due to a rebuilding of the pilot plant reactor it was possible to perform this experiment. Moreover, the experiment was done before the reactor was charged with slag and therefore no freeze lining was present. Water was charged to the pilot plant reactor so that it was partially filled. During the experiment, the conductivity was measured in the water with submerged gas blowing before, during and after a 20wt% NaCl solution was added. The experimental setup can be seen in figure 9 and more information is found in table 3.

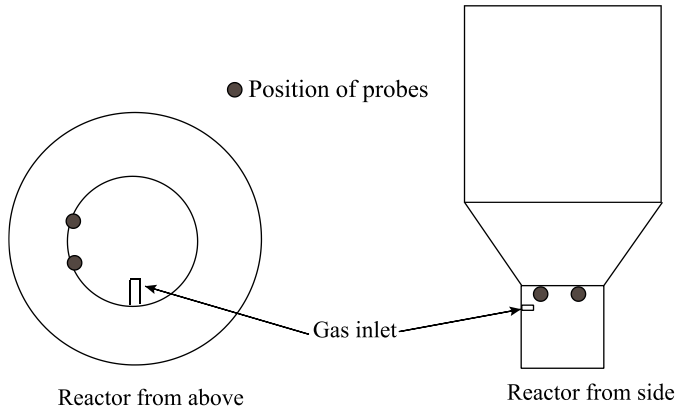


**Figure 8. Position of conductivity probes in the IronArc pilot plant reactor.**

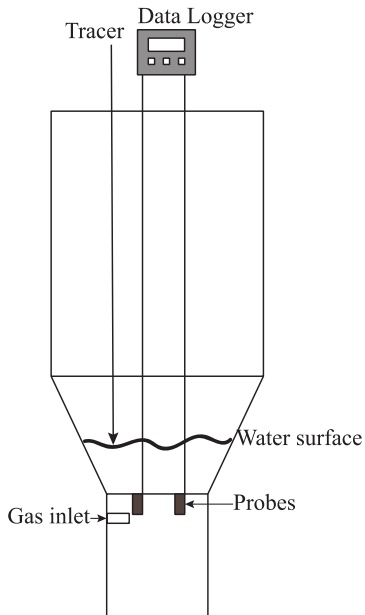


**Figure 9. Experimental setup for the conductivity measurements performed in the IronArc pilot plant reactor**

The mixing times to reach both 95% and 99% degrees of homogenization were determined based on the average time for both probes to reach the particular degree of homogenization, according to equation (11):

$$t_{mixing} = \frac{t_{p1} + t_{p2}}{2} \quad (11)$$

where  $t_{mixing}$  is the mixing time,  $t_{p1}$  is the mixing time for probe 1, and  $t_{p2}$  is the mixing time for probe 2.

**Table 3: Setup for industrial mixing time test by conductivity measurements**

Amount	Amount	Amount of water	Flow rate
water(l)	NaCl(g)	solvent(l)	(Nm <sup>3</sup> /h)
<b>~740</b>	2400	10	230

## 2.2. NUMERICAL MODEL

To describe the interface between the injected gas and the liquid the interface for the penetration depth predictions both the EE (Eulerian multiphase model) and VOF (Volume of Fluid) model were used. The predictions for the small-scale model was compared to both the EE and VOF calculations. To describe the interface between the gas and liquid for the mixing time calculations an Eulerian multiphase model was used. For the mixing time calculations, a species transport model was used to simulate the tracer in the domain.

### 2.2.1 ASSUMPTIONS

The flow phenomena in this process are very complex. Therefore, assumptions were made in order to reduce the complexity of the numerical calculations and predictions. The following assumptions were made for the small-scale physical model and the model based on the pilot plant:

- Small scale models (mixing time and penetration depth)
  1. The water and air are regarded as Newtonian fluids
  2. The flow in the model is isothermal.
  3. The water and injected air are incompressible fluids.
  4. In the numerical simulation that uses the Eulerian multiphase, the model bubble diameter is assumed constant to simplify the model. Deformation of the gas bubbles is not considered, so the gas

bubbles are assumed to be spherical and their interactions regarding bubble breakup and coalescence have been neglected.

5. It is assumed that the addition of tracer does not affect the flow field in the process.
- IronArc Pilot plant models (mixing time and penetration depth)
    1. The slag and injected gas are regarded as Newtonian fluids
    2. The slag and injected gas are incompressible fluids.
    3. Since the injected gas consists of approximately 20 times more air than LPG, the injected gas was assumed to have the properties of air.
    4. The air was assumed to obtain the slag temperature momentarily.
    5. The flow in the model is assumed to be isothermal.
    6. The properties of the gas and slag were those at a temperature of 1600°C, since that is the approximate temperature of the slag.
    7. The effect of chemical reactions between the injected gas and the slag is not considered in the calculations.
    8. The bubble diameter is assumed constant to simplify the model. Deformation of the gas bubbles is not considered, so the gas bubbles are assumed to be spherical and their interactions regarding bubble breakup and coalescence have been neglected.
    9. It is assumed that the addition of tracer does not affect the flow field in the process.

## 2.2.2 MULTIPHASE THEORY

### 2.2.2.1 VOF MODEL

To describe the interface and its movement between the injected gas and the liquid phase, the volume of fluid (VOF) model was used. It tracks the interface by using a scalar quantity for the volume fraction of the phases in each cell. The continuity with VOF, which is solved for each phase, in these cases the gas and liquid, is expressed as follows:

$$\frac{\partial \alpha_q \rho_q}{\partial t} + \vec{v} \cdot \nabla (\alpha_q \rho_q) = 0 \quad (12)$$

where  $\alpha$  is a scalar quantity that describes the volume fraction of the  $q$ :th phase and the constraint on which the primary phase will be computed is stated as follows:

$$\sum_{q=1}^n \alpha_q = 1 \quad (13)$$

Throughout the domain a single momentum equation is solved and the resulting velocity field is shared for the phases. The momentum equation is dependent on the volume fraction of the different phases through the viscosity and density.

$$\begin{aligned} \frac{\partial(\rho \vec{v})}{\partial t} + \vec{v} \cdot \nabla(\rho \vec{v}) \\ = -\nabla p + \nabla \cdot [\mu(\nabla \vec{v} + \nabla \vec{v}^T)] + \rho \vec{g} + \vec{F} \end{aligned} \quad (14)$$

The density and viscosity are calculated in each control volume as shown below:

For the density,

$$\rho = \alpha_l \rho_l + (1 - \alpha_l) \rho_g \quad (15)$$

and viscosity,

$$\mu = \alpha_l \mu_l + (1 - \alpha_l) \mu_g \quad (16)$$

where the subscripts  $l$  and  $g$  represent the liquid and gas, respectively. Due to turbulence, additional scalar equations were solved, for  $k$  and  $\epsilon$ . [16, 65]

### 2.2.2.2 EULERIAN MULTIPHASE MODEL

For the Eulerian multiphase model, the different phases are treated as interpenetrating continua and a set of equations are solved for each phase. Both phases are treated as continuous media and are averaged over each control volume. Furthermore, both continuity and momentum equations are solved for each phase and a single pressure is shared between the phases. The momentum transfer between the gas and water is modeled by using a drag term. A diameter is set for the secondary phase, which in this case is the dispersed gas bubbles. The turbulence is calculated per phase and both phases are considered to be incompressible.

The Eulerian multiphase model:

The continuity equation for the Eulerian multiphase model reads as follows:

$$\frac{1}{\rho_{rq}} \left( \frac{\partial}{\partial t} (\alpha_q \rho_q) + \nabla \cdot (\alpha_q \rho_q \bar{\mathbf{v}}_q) \right) = \sum_{p=1}^n (\dot{m}_{pq} - \dot{m}_{qp}) \quad (17)$$

where  $\bar{\mathbf{v}}_q$  is the velocity of phase  $q$  and  $\dot{m}_{pq}$  represents the mass transfer from the  $p^{th}$  to  $q^{th}$  phase, and  $\dot{m}_{qp}$  represents the mass transfer from phase  $q$  to phase  $p$ .  $\alpha_q$  is the volume fraction of phase  $q$  and  $\rho_q$  is the density of the  $q^{th}$  phase. The parameter  $\rho_{rq}$  is the volume averaged density of the  $q^{th}$  phase in the solution domain.

The momentum equation for phase  $q$  may be expressed as follows:

$$\begin{aligned} & \frac{\partial}{\partial t} (\alpha_q \rho_q \bar{\mathbf{v}}_q) + \nabla \cdot (\alpha_q \rho_q \bar{\mathbf{v}}_q \bar{\mathbf{v}}_q) \\ &= -\alpha_q \nabla p + \nabla \cdot \bar{\bar{\boldsymbol{\tau}}}_q + \alpha_q \rho_q \bar{\mathbf{g}} \\ &+ \sum_{p=1}^n (K_{pq} (\bar{\mathbf{v}}_p - \bar{\mathbf{v}}_q) + \dot{m}_{pq} \bar{\mathbf{v}}_{pq} \\ &- \dot{m}_{qp} \bar{\mathbf{v}}_{qp}) + \bar{\mathbf{F}}_q \end{aligned} \quad (18)$$

where  $\bar{\bar{\boldsymbol{\tau}}}_q$  the  $q^{th}$  phase stress strain tensor,  $\bar{\mathbf{F}}_q$  is an external body force between the different phases,  $\bar{\mathbf{v}}_{pq}$  is the interphase velocity and  $\bar{\mathbf{g}}$  is the gravitational acceleration constant.  $K_{pq}$  is an exchange coefficient between the phases and  $p$  is the pressure shared by the phases. The general form of the  $K_{pq}$  is defined as follows:

$$K_{pq} = \frac{\rho_p f}{6\tau_p} d_p A_i \quad (19)$$

where  $\rho_p$  is the density of phase  $p$ ,  $\tau_p$  is the particulate relaxation time,  $A_i$  the interfacial area and  $f$  is the drag function. The drag function is defined as follows:

$$f = \frac{C_D Re}{24} \quad (20)$$

where  $Re$  is the Reynolds number and  $C_D$  is the drag coefficient. In this case, the drag coefficient from the Schiller Naumann Model is used. [65-67]

### 2.2.2.3. TURBULENCE THEORY

The Realizable  $k$ - $\varepsilon$  model was used to describe the turbulence in the domain:

The turbulent viscosity is calculated by combining  $k$  and  $\varepsilon$  and is defined as follows:

$$\mu_t = C_\mu \frac{k^2}{\varepsilon} \quad (21)$$

where  $k$  is the turbulent kinetic energy,  $\varepsilon$  is the rate of dissipation of turbulent kinetic energy and  $C_\mu$  is a constant for the turbulent viscosity. The transport equations for  $k$  and  $\varepsilon$  are defined as follows:

$$\begin{aligned} \frac{\partial(\rho k)}{\partial t} + \frac{\partial(\rho k u_j)}{\partial x_j} \\ = \frac{\partial}{\partial x_j} \left[ \left( \mu + \frac{\mu_t}{\sigma_k} \right) \frac{\partial k}{\partial x_j} \right] + G_k + G_b - \rho \varepsilon \\ - Y_M + S_k \end{aligned} \quad (22)$$

and

$$\begin{aligned} \frac{\partial(\rho \varepsilon)}{\partial t} + \frac{\partial(\rho \varepsilon u_j)}{\partial x_j} \\ = \frac{\partial}{\partial x_j} \left[ \left( \mu + \frac{\mu_t}{\sigma_\varepsilon} \right) \frac{\partial \varepsilon}{\partial x_j} \right] + \rho C_1 S_\varepsilon \\ - \rho C_2 \frac{\varepsilon^2}{k + \sqrt{\nu \varepsilon}} + C_{1\varepsilon} \frac{\varepsilon}{k} C_{3\varepsilon} G_b + S_\varepsilon \end{aligned} \quad (23)$$



Where  $G_b$  is the production of turbulence kinetic energy due to bouancy,  $\sigma_k$  is Prandts constant for the turbulent kinetic energy,  $\sigma_\varepsilon$  is Prandts constant for the dissipation rate of turbulent and  $G_k$  is the production of turbulent kinetic energy due to mean velocity gradients and it is defined as follows:

$$G_k = -\rho \overline{u'_i u'_j} \frac{\partial u_j}{\partial x_i} \quad (2)$$

#### 2.2.2.4 SPECIES TRANSPORT MODEL

The mixing, and in turn the mixing time, in the bath of the process reactor was calculated by using the species transport model. The following equations were solved for the species transport model in the bath:

$$\frac{\partial(\rho Y)}{\partial t} + \nabla \cdot \rho \bar{\mathbf{v}} Y = -\nabla \cdot \bar{\mathbf{J}} \quad (25)$$

where  $Y$  is the mass fraction of species and  $\mathbf{J}$  is the diffusion flux of species. Also, for turbulent flows the diffusion is calculated as follows:

$$\bar{\mathbf{J}} = -\left(\rho D_m + \frac{\mu_t}{Sc_t}\right) \nabla \cdot Y \quad (26)$$

where  $D_m$  is the mass diffusion coefficient for species  $SC_i$  is the turbulent Schmidt number,  $\mu_t$  is the turbulent viscosity.

#### 2.2.3 BOUNDARY CONDITIONS AND SOLUTION METHODS

##### 2.2.3.1 VALIDATION CASE (PENETRATION DEPTH & MIXING TIME)

All boundary conditions for the penetration depth validation case simulation corresponded to the experimental procedure from the small-scale physical water experiment, where air was injected into the water from the nozzle. The speed of the air at the inlet was 113 m/s (Mach 0.33). In addition, the flow was assumed to be incompressible. In the mathematical model the volume fraction of air at the inlet exit was set to 1 and a velocity inlet was used as boundary condition for the gas injection at the inlet. At the water surface a pressure condition equal to atmospheric pressure was

used. The walls were treated as stationary walls with a no-slip condition and standard wall functions were used. The geometry with the inlet and outlet boundaries of the numerical domain can be seen in Figure 10.

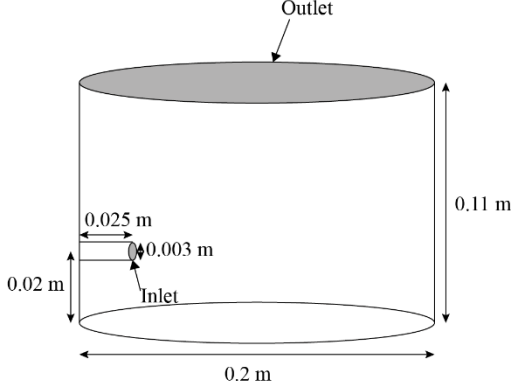


**Figure 10: Geometry of the water model domain.**

The computational domain was created by using a 3D mainly hexahedral mesh. To reduce the computational expense for the simulations, the mesh was refined in the area of the gas plume where the velocity and volume fraction gradients were high. A cross section of the medium mesh and the refined area can be seen in Figure 11. The pressure-velocity coupling was solved by using the PISO algorithm. For the spatial discretization the gradients were computed by using the least square cell-based method. The second order upwind scheme was chosen for momentum and first order upwind for the turbulent kinetic energy in the spatial discretization. A variable time step was used for the simulation with a global courant number of 2 for the VOF simulations.

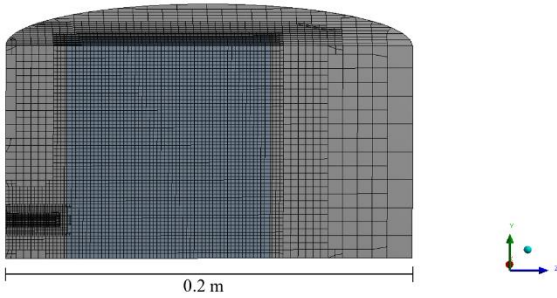


**Figure 11: Medium mesh at a cross section plane of the domain.**

The boundary conditions of the numerical model (for the mixing time) correspond to the experimental setup, which are given in table 1. Air was injected into the water through the nozzle. The speed of the air at the inlet of the nozzle was  $44 \text{ ms}^{-1}$  (Mach 0.13), when accounting for the measured and controlled gas flow rate and diameter of the nozzle. The flow was assumed to be incompressible due to the low Mach number, based on previous experience from the pilot plant trials. In the mathematical model, the volume fraction of air at the inlet exit was set to 1 and a mass flow inlet was used as boundary condition for the gas injection. Also, a pressure outlet with a pressure condition equal to the atmospheric pressure was used at the top of the domain, i.e. the top part of the reactor. The walls were treated as stationary walls having a no-slip condition and standard wall functions were used.

A 3D hexahedral mesh was used (in most parts of the domain). One of the main functions with this mesh is the large number of hex cells. The simulations were run in transient mode, due to the turbulent flow in the bath which was clearly visible in the experimental setup. The tracer was patched into the domain and was added into the bath after 30 seconds of stirring. Specifically, this time represents a time several times longer than the measured mixing time. In this way, it was ensured that the bath had reached a fully developed flow before a tracer was added. The pressure velocity coupling was solved with the spatial discretization the least square cell-based method. Also, a constant time step of 0.0001 was used throughout the entire simulation of the mixing time.

### 2.2.3.2 IRONARC (PENETRATION DEPTH AND MIXING TIME)

The geometry for the numerical domain was the same scale as the existing pilot plant. To reduce the simulation cost, the top part of the reactor was removed. The geometry for the IronArc domain can be seen in Figure 12.

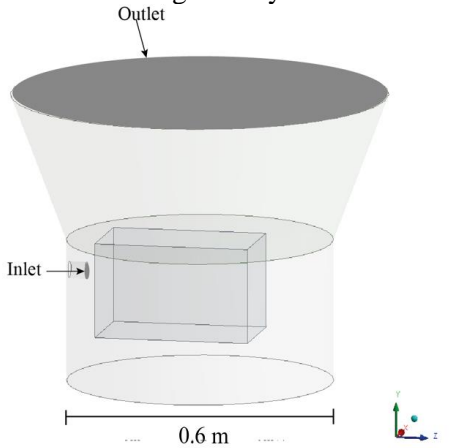


**Figure 12: Numerical domain of the IronArc pilot plant simulation.**

Gas was injected into the slag through a nozzle placed at the side wall. Since the injected gas consists of approximately 20 times more air than LPG, the injected gas was assumed to have the properties of air. Furthermore, the air was assumed to obtain the slag temperature momentarily and therefore, the properties of the gas and slag were those at the temperature of 1600°C since that is the approximate temperature of the slag. The slag was assumed to consist of iron oxides. A mass flow rate was used as a boundary condition at the inlet. This corresponds to a velocity of 450 m/s, which is below Mach 1 at the temperature of 1600 °C temperature and therefore it was assumed that the flow was incompressible. The gas density was assumed to be constant during the simulations and the values at the operating temperature were calculated by using the ideal gas law. Also, the simulations were performed under isothermal conditions (1600°C).

For the mixing time calculations, the domain is larger compared to the penetration depth and it includes the slag surface. The tracer in this case had the same properties as the slag and it was patched at the same location (approximately) where the tracers were added in the water model experiments. Similarly, the measurement points in the gas-slag simulation were similar as the location of the probes in the water model experiment.

## 3. RESULTS AND DISCUSSION

### 3.1. EXPERIMENTAL PART

#### 3.1.1 SMALL SCALE WATER MODELING (SUPPLEMENT 1)

##### 3.1.1.1 MIXING TIME

Figure 13 shows the mixing time that was measured when using a flow rate of  $282 \text{ NLmin}^{-1}$ . This value corresponds to a flow rate of  $265 \text{ Nm}^3\text{h}^{-1}$ , which is the average flow rate used in the pilot plant reactor. In total, six trials were performed using this experimental setup.

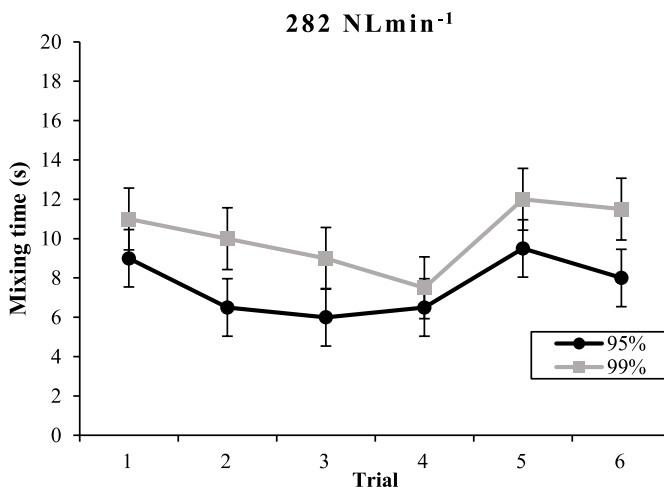
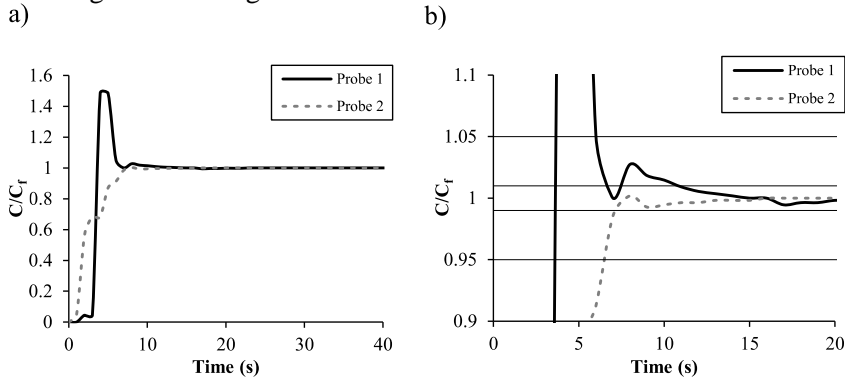


**Figure 13.** Measured mixing times for a flow rate of  $282 \text{ NLmin}^{-1}$  for both a 95% and a 99% degree of tracer homogenization. Data are given for 6 trials.

This figure shows the six repeated trials focusing on mixing time measurements, when using one inlet and the setups shown in figure 5 and figure 6 a). Tracer additions were made at approximately the same position in the bath for all trials. The time to reach both 95% as well as 99% homogenization degrees in the water bath, as defined in Equation (9), were determined. As expected, the mixing time was shown to be 34% longer when comparing the average mixing time for all cases for both homogenization degrees, for a 99% homogenization degree compared to a 95% homogenization degree. This trend was found for all trials. For a 95%

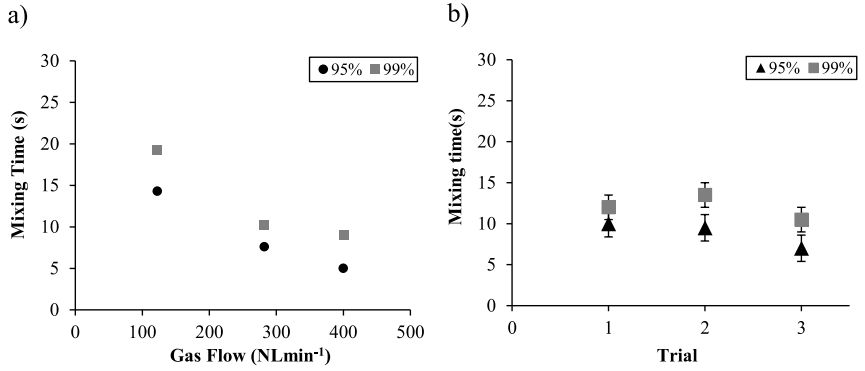
homogenization degree, the mixing time varies between 9.5 s and 6 s with an average mixing time of 7.6 s. Moreover, the results for a 99%-degree homogenization degree are 12 and 7.5 s, for the maximum and minimum values, respectively. Furthermore, the average value is 10.2 s.

A typical tracer concentration curve can be seen in figure 14 a). It shows the normalized tracer concentrations for the two probes in the water after an addition of the saline solution. In figure 14 b), the same curve is shown but for a narrower interval. Thereby, it is possible to better observe at which time the tracer concentration reached the homogenization degrees of 95% and 99%. During the measurements the flow in the water bath was strong and turbulent. Also, periodic circular movements of the bath could be observed at the wall of the reactor model. Due to this circulating movement of the bath surface, the irregularity of the surface waves and in turn the change of bath height it is difficult to guarantee a completely similar situation during the tracer addition for each trial. However, this powerful stirring also gave rise to a mixing time below 10 seconds for a 95% degree of homogenization.



**Figure 14: Data of normalized conductivity curves for two probes. These measurements were taken from the third trial when using one gas inlet. a) Shows the normalized conductivity values from 0 to 1.6. b) Shows the normalized conductivity values from 0.9 to 1.1. Horizontal lines that shows the areas for 95% and 99% degrees of homogenization are also shown.**

Figure 15 a) shows the mixing times for three different flow rates, namely 122, 282 and 400 NLmin<sup>-1</sup>. These results also show that an increase in flow rate leads to a decreased mixing time, which is expected due to an increase in velocity and buoyancy effect of the injected gas. This has been shown in earlier studies.[36]



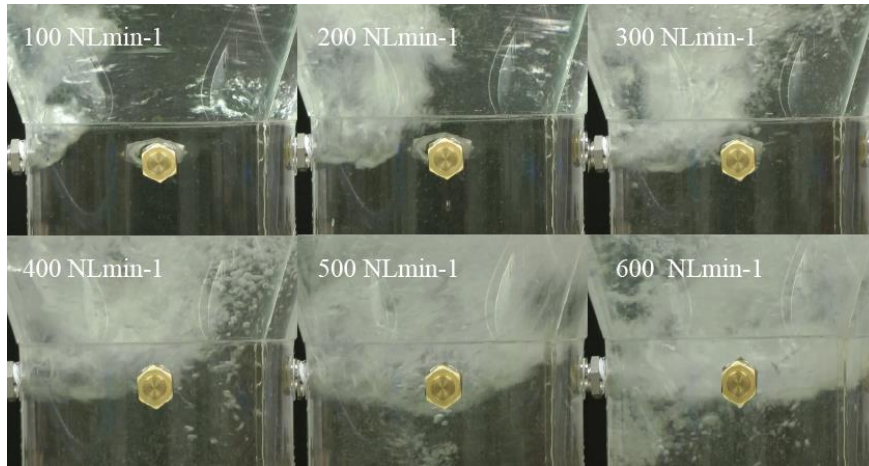
**Figure 15. a) Mixing times for experiments using different flow rates when using one gas inlet. b) Mixing times for experiments using three gas inlets and the same flowrate. Data are presented for both 95% and 99% homogenization degrees.**

Figure 15b) shows the effect of the tuyere number on the mixing time, which was determined for a gas flow rate of 282 NLmin<sup>-1</sup> (same flowrate for all trials). Three tuyeres were used and each had a diameter of 0.0117 m. The probe positions were the same as in Figure 6 a) and the tracer was added at approximately the same place as in the trials using one inlet. The positions of the gas inlet and the conductivity probes can be seen in Figure 4 b). The tracer position during addition varied in an area with a radius of approximately 3 cm. The purpose of these trials was to investigate if the number of nozzles have an impact on the mixing time. The results show that the mixing time significantly increases in the case with 3 tuyeres compared to the case with 1 tuyere. The increases were 15.8% and 17.6%, for a 95 % homogenization degree and a 99% homogenization degree, respectively. The corresponding mixing times were 8.8 (95% degree of homogenization) and 12 seconds (99% degree of homogenization). A possible explanation is that the surface was much calmer in the case when using 3 inlets compared to when using one inlet. The circular movement, in the one inlet case, will influence the stirring of the bath and make the tracer distribution in the bath faster. Furthermore, it will result in an increased radial velocity and horizontal flow in the bath. This theory is supported by another investigation [18], which showed that the mixing time decreases when a horizontal submerged gas injection is inserted into a top and bottom blown converter. This decrease may be due to the side blowing, which in turn increases the bath mixing and reduces the mixing time. It is not common that the effect of the tuyere number on the mixing time has been investigated. In an earlier experiment [21], the influence of the nozzle number on the mixing time for a small scale oblong AOD converter was investigated. The results showed that the number of tuyeres has an insignificant effect on the mixing time, when comparing 6 and 8

tuyeres for gas blowing positioned at the same side of the converter. For the 3-inlet case in the present work, two of the tuyeres were placed at positions direct opposite to each other and on different sides of the model. Therefore, they work as a counterpart to each other so that the circular movement of the surface is greatly reduced. With the same flow rate for the three-inlet case, the flow rate per inlet was one third compared to when only one inlet was used. This resulted in a velocity of 14,7 m/s compared to 44m/s for the one-inlet case. This resulted in a shorter penetration depth of the air into the water for the three-inlet case compared to the one-inlet case.

### 3.1.1.2 PENETRATION DEPTH

The penetration depth was determined (at several flow rates) in the water model by taking photographs and filming with a high-speed camera and a video camera. This is illustrated in Figure 16, where the penetration of the gas and the gas plume are seen for the measured flow rates. In Figure 17, the penetration depths at different flow rates from the experiments are compared to predictions using an empirical equation from literature [34]. It was observed that the penetration depth did not have a constant value, but instead showed a sort of pulsating behavior. These different pulses penetrated different distances into the water, which have been reported earlier [38]. This is illustrated in Figure 17, which shows the minimum and maximum penetration depths at each tested flow rate and the predicted penetration depth calculated by using equation (27). These pulses appear less than a second apart from each other and are therefore difficult to detect when observing the flow without using a high speed camera, but are nonetheless visible.



**Figure 16. The measured air plume in the water for all tested flowrates.**



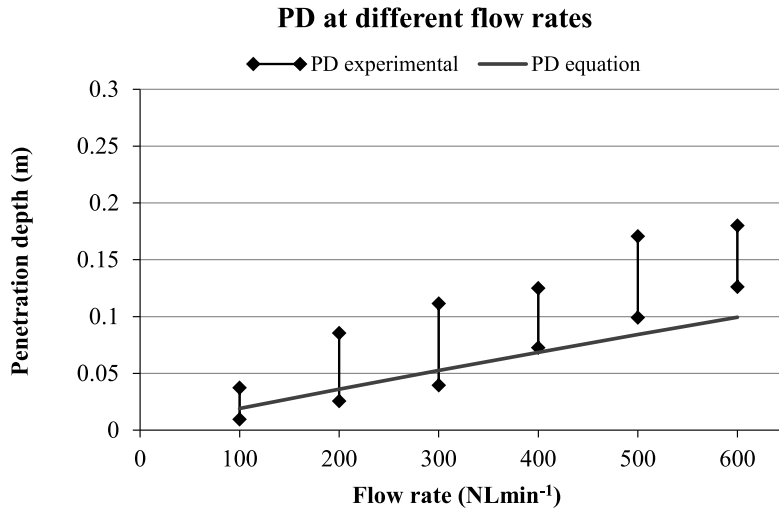


**Figure 17. Penetration depths determined both experimentally and using the empiric equation at different flow rates. The experimental lines show the max and min values at each flow rate.**

Figure 18 shows the flowrates for the approximate max and min penetration depths captured at different pulses for a flowrate of 400 NLmin<sup>-1</sup>. The length of penetration differs clearly, from the minimum value of 7.3 cm to the maximum value of 12.5 cm. When comparing the experimental results to the predictions using the empirical equation, the lower penetration depth values seems to fit the empirical equation (10) better for gas flow rate values of up to around 400 NLmin<sup>-1</sup>. However, for flow rates from 500 NLmin<sup>-1</sup> up to 600 NLmin<sup>-1</sup> the penetration depths from the experiments differs, more clearly, from the penetration depths from the empirical equation, even for the shortest pulses. Also, the pulses were seen more clearly for a higher flowrate compared to a lower flow rate.

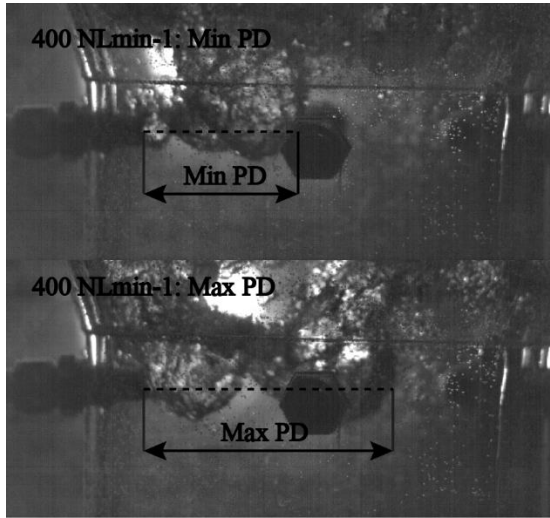


**Figure 18.** The penetration of the air in the water for a flowrate of  $400 \text{ NLmin}^{-1}$ . Data are presented for the minimum penetration (upper figure) and the maximum penetration (lower figure).

Both the experiments and the predictions expressing the same tendency showing that an increased gas flow rate results in an increased penetration depth. This is expected, due to that the gas will have a higher velocity at the inlet for an increased flow rate. Also, the pulses were more visible and more accurately determined lengthwise for the shorter penetration depth as well as for the lower flow rates, compared to the pulses found at the higher flowrates. In the latter case, the air from the longer penetration of a pulse were still in front. Furthermore, they rose more slowly in the vertical direction than for the next following shorter pulse, which penetrated the water horizontally. Overall, the empirical equation (equation 10) is, according to these results, more fitted to use for lower Froude numbers than for higher Froude numbers.

The reflections from the curved cylindrical shape of the water model were reduced by an outer box made of acrylic plastic, which was filled with water. This gives a more representative vision of the plume compared to when observing the plume through the curved glass wall.

The scaled value from the average flow rate of the pilot plant reactor the flow rate off  $300 \text{ NLmin}^{-1}$  is just a little bit larger than  $282 \text{ NLmin}^{-1}$ , which corresponds to the scaled average flow rate of the pilot plant reactor. This means that according to this result, the penetration depth corresponding to the pilot plant flow rate would be slightly lower than the penetration depth

span of 0.04-0.011 m for the 300 NLmin<sup>-1</sup> flow rate. Therefore, the gas plume will not rise at the opposite wall. Hence, the refractory wear should be less on that wall compared to a case with a longer penetration depth. Also, since there are some distances between the same walls as the gas is injected from, the plume will not rise directly at the tuyere wall. Reducing the refractory wear. The energy usage in the gas is also affected in a positive way if the gas plume rises at a distance away from the wall, since a larger volume of the plume will be used to stir the bath.

### 3.1.2 PILOT PLANT TRIALS (SUPPLEMENTS 3 & 5)

#### 3.1.2.1 MIXING TIME

##### 3.1.2.1.1 SLAG-GAS (SUPPLEMENT 3)

The results of the pilot plant trial experiments can be seen in figures 19, 20, 21 and 22. The results for trials 1 and 2, are shown in figure 19. The powder (6.4 kg MnO<sub>2</sub>) was added after the reference samples were taken for both trials. For trial 1 it was added between samples 2 and 3 and for trial 2 the tracer powder was added between samples 15 and 16. After the MnO<sub>2</sub> powder was added, the MnO content increased from around 0.13% to just above 0.4%. Thereafter, it stayed steady at that MnO amount for all samples taken during trial 1. Similar results were found for trial 2. Since the sampling interval was one minute, the results from both trials show that the mixing times were equal to or less than one minute. Only small deviations existed between all the MnO contents for all the samples taken after a tracer addition in trial 1 as well as in trial 2, which can be seen table 4. The standard deviation for trial 1 (samples 3 - 12) was 0.00738 and for trial 2 it was 0.0165. This means that the sample data lies very close to the mean value of 0.419 within 3 % for trial 1 and within 4% for the mean value of 0.655 for trial 2. Also, the standard errors in both trials were also low, namely 0.00233 and 0.00521 for respective trial. Overall, this shows that there is a relatively small spread in the sampling distribution and that the measurements of the MnO content in the samples are reliable.

**Table 4: Shows the standard deviation, average value and the standard error of the samples with 1-minute interval, for trial 1 and trial 2.**

	<b>Trial 1 (samples 3-12)</b>	<b>Trial 2 (samples 16-25)</b>
<b>STD</b>	0.00738	0.0165
<b>Average (%)</b>	0.419	0.655
<b>Standard error</b>	0.00233	0.00521

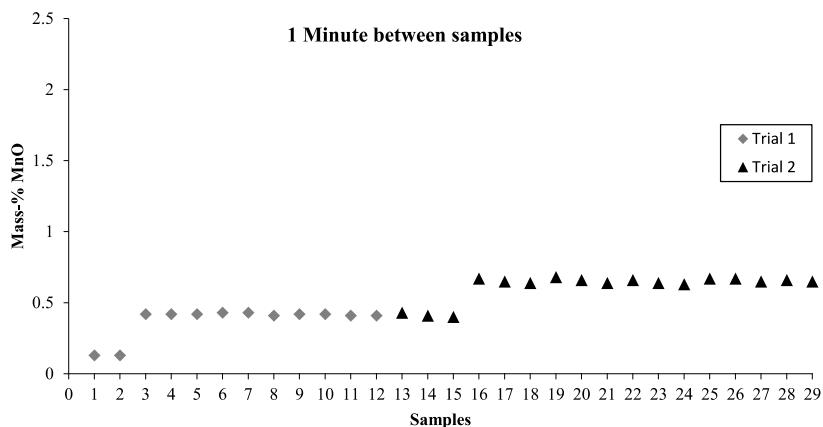


**Figure 19: Content MnO (%) for the different samples for trial 1 and trial 2, respectively. The MnO<sub>2</sub> powder was added after sample 2 for trial 1 and after sample 15 for trial 2.**

The total amount of MnO in the slag was compared to the theoretical amount for trials 1 and 2. These calculations can be seen in table 5. The total amount of MnO in the slag is the amount of MnO according to the chemical composition (the average value from an XRF analysis) of the slag with a mass of 1300 kg. The theoretical value of the total amount of MnO in the slag is based on mole relation calculations between MnO and MnO<sub>2</sub>. It represents the amount of MnO in the slag that can be formed from the added MnO<sub>2</sub> powder. There is a 27% difference between the total theoretical amounts of MnO in the slag and the total amount of measured MnO in the slag. The XRF determinations of the chemical composition of the slag shows some uncertainties, but since the standard deviations and the standard errors are small this uncertainty is assumed to be small. Since the powder were added from the top of the reactor in cans, a likely explanation to the lower amount of MnO in the slag is that some of the powder exited through the off-gas pipe before the remaining part of the powder entered the slag.

**Table 5: Shows the initial amount of MnO, the added amount of MnO<sub>2</sub>, the total amount of MnO and theoretical amount of MnO in the slag, for the two trials performed.**

<b>Trial 1</b>			
Initial amount of MnO in slag (kg)	Added MnO <sub>2</sub> (kg)	Tot. MnO in slag (kg)	Tot. MnO in slag theory (kg)
1.69	6.4	5.447	6.913
<b>Trial 2</b>			
Initial amount of MnO in slag (kg)	Added MnO <sub>2</sub> (kg)	Tot. MnO in slag (kg)	Tot. MnO in slag theory (kg)
5.447	6.8	8.544	10.996

The results of trials 3, 4 and 5 can be seen in figure 20, 21 and 22, respectively. These figures show the amount of MnO for the different samples. The trend, in these trials, is that the content of MnO increases almost instantly. Furthermore, this increase can be seen in the first sample taken after a tracer addition, (sample 3). In figure 20 which represents trial 3, the third sample is taken 8 seconds after the tracer addition. A value of 1.46% MnO is measured for this sample after 8 seconds. Overall, this is the sample with the lowest MnO content. Thereafter, the MnO content in sample 4 is increased to 1.67% with a maximum value of 1.7% during tapping. According to this trial, the slag is likely homogenized already after the first 8 seconds, but completely homogenized when the fourth sample is taken after 16 seconds. The difference between the fourth sample and the tapping sample (sample 7, which was taken after several minutes) differ by only 0.03% MnO. It should also be mentioned that the time for taking the fourth sample (8 seconds for trial 3) is an approximate value. Firstly, the tracer powder was added in 3 bottles that could not be charged at the same time. This was due to a too small feeding hole that would only allow one bottle at the time to be fed through the hole in the roof. This means that there is sometimes, only a couple of seconds are available, for feeding of the material. Overall, the first sample for trials 3, 4 and 5 shows similar tendencies, namely that there is a fast increase of the MnO content. Moreover, the mixing is fast, and that the slag gets homogenized in just a few seconds. The homogenization for trial 4 is likely completed in sample 4, which corresponds to a mixing time of approximately 7 seconds. This means that the trend for the experiments is clear. It shows that there is an increase in the MnO content already after the second sample (after an addition of tracer) is taken. Thus, this result indicates that the mixing is almost instant.

The maximum deviation between the largest and smallest values obtained for the measured values are around 6%. It shows that the homogenization of the tracer happens in a short time and that the deviation is not since the tracer has not been homogenized within the melt. It is more a general deviation that is seen in basically all slags. A slag is often not 100% homogeneous and the composition at a fixed point differs slightly over time. In this case one reasons may be the freeze lining, where a part of the slag can melt the freeze lining creating a difference in composition. These results give an even clearer picture of the fast sampling and confirms the results of trials 3, 4 and 5.

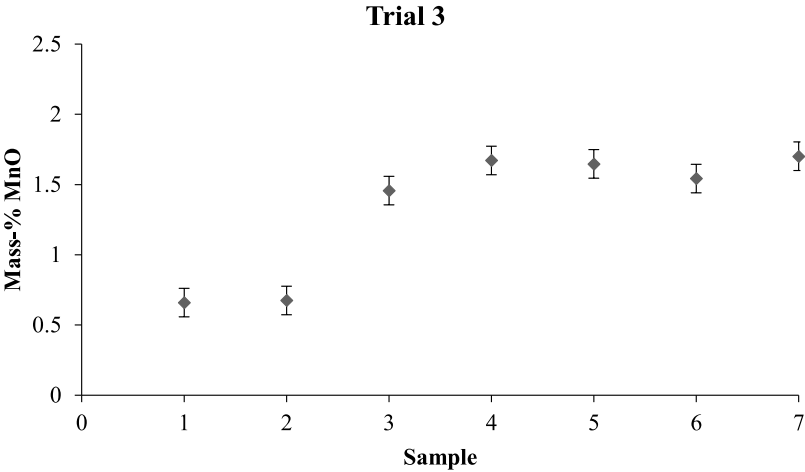


**Figure 20 MnO (%) content for all the sample taken during the sampling for trial 3, where samples 1 and 2 are taken before a tracer addition and the rest of the samples are taken after an addition of the MnO<sub>2</sub> tracer powder.**

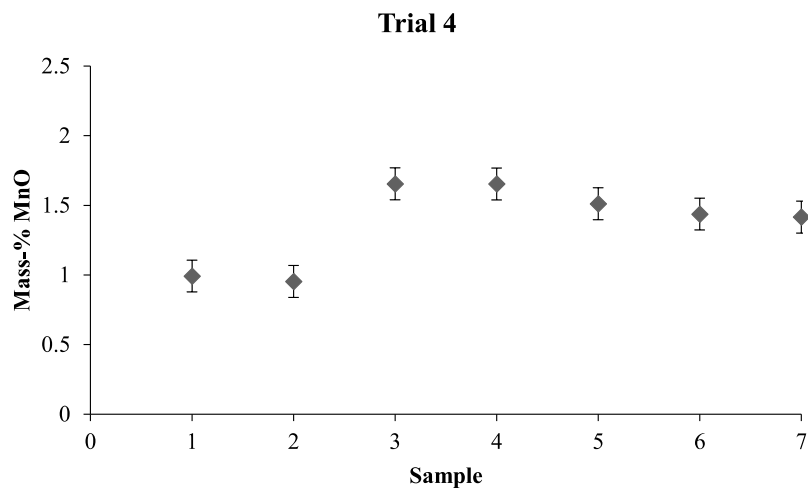


**Figure 21:** MnO (%) content for all the sample taken during sampling in trial 4, where samples 1 and 2 are taken before a tracer addition and the rest of the samples are taken after a tracer addition.

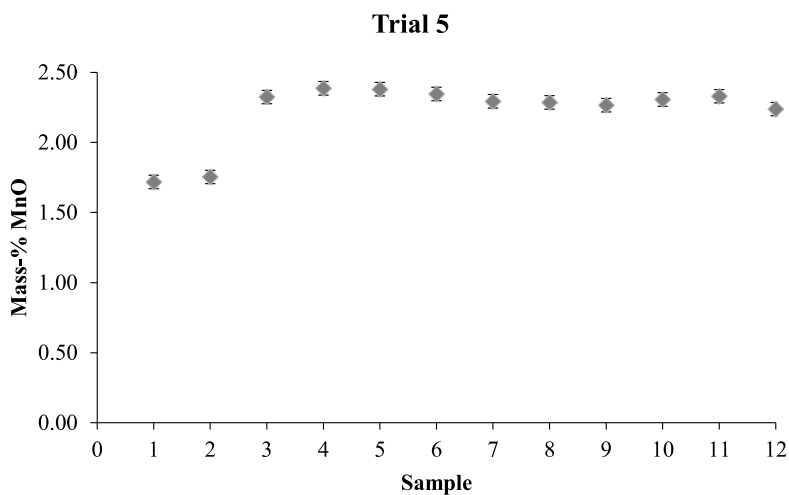


**Figure 22:** The amount of % MnO in each slag sample taken during the pilot plant experiment.

### 3.1.2.1.2 SLAG INVESTIGATION

#### 3.1.2.1.2.1 LOM

In figure 23, a LOM picture of a cross section of a slag sample quenched in air can be seen. A larger piece of the slag is seen in figure 24. The different numbers in figure 23 represents different zones in the slag sample. Zone number 1 represents the slag surface of the sample and the part of the slag that has been cooled the fastest. It can be seen that the microstructure is really fine, which indicates that it has been cooled fast and that no individual particles can be seen. Normally, it is clearly seen when solid particles are present in the structure, they are not part of the solidification process. However, no solid particles are seen in this sample and this zone is quite homogeneous. In zone 2, some precipitations are seen because of the slower cooling compared to zone 1. But the entire zone 2 show a similar microstructure except for some pores. Zone 3 represents the pores in the sample. No particles can be seen in zone 2 either. Zone 4 is simply the Bakelite holding the sample together. The small differences in microstructure between zones 1 and 2 likely happened due to the different cooling rates in the different zones. Therefore, no individual particles can be seen. Thus, it can be concluded that a large majority of the solidified slag was in a liquid state before it was cooled. It is also seen in figure 24 that in a macro perspective it looks like a liquid slag that has solidified. This is important to know, since a presence of solid particles in the slag would result in a two-phase slag and a higher viscosity than the theoretic value. This, in turn, would suggest a different behavior of the slag. Specifically, it would most likely not behave like a Newtonian fluid. The results from the LOM investigation showed that no individual particles present in the microstructure, which were not part of the solidification process of the slag. Hence, the slag can be assumed to be in a liquid state during the operation of this process. Furthermore, this means that it is possible to get an estimation of the viscosity of the slag.



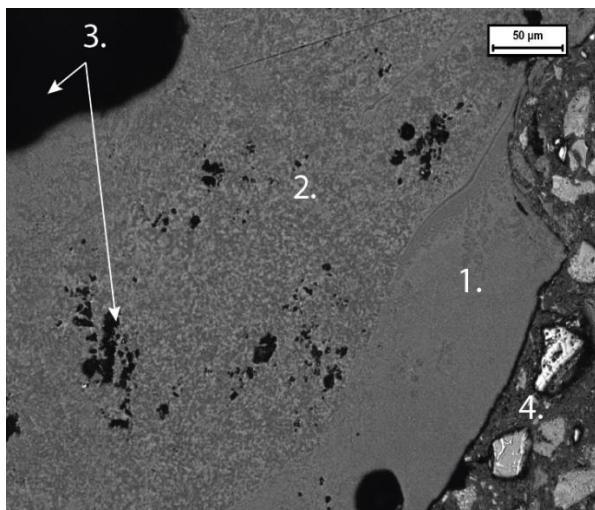


**Figure 23: LOM picture of 2D cross section surface of slag sample. The numbers represent different zones in the sample.**



**Figure 24: A piece of solidified slag from a macro perspective.**

### 3.1.2.1.2.2 THERMO-CALC CALCULATIONS

Thermo-Calc calculations were performed for trials 1 to 5 and for respective slag composition. The normalized composition of the slags used in the trials can be seen in table 6. Elements larger than 1 mass-% were included in the Thermo-Calc calculations. The database TCOX7 were used, which includes 18 elements and is intended to be used for solid or liquid sulfides

or oxides and to be used for slag calculations as well as for other applications [63]. This was done in order to investigate the phases of the slag during the operational conditions theoretically from a thermodynamic perspective. Furthermore, to investigate the amount of liquid phase of the slag and to get an in-depth knowledge to strengthen the earlier graphically presented LOM results.

**Table 6: Normalized slag composition for the different trials. The number of elements in the slag is also shown, since not all these composition values were not included in the table due to the low amount per element. Nr stands for the number of elements.**

<b>Trials (mass%)</b>	<b>CaO</b>	<b>MgO</b>	<b>SiO<sub>2</sub></b>	<b>Al<sub>2</sub>O<sub>3</sub></b>	<b>FeO</b>	<b>NiO</b>	<b>MnO</b>	<b>Nr</b>
<b>1 &amp; 2</b>	2.8	1.5	36.2	5.0	54.4	-	-	20
<b>3</b>	34.2	15.8	34.6	12.9	2.5	-	-	28
<b>4</b>	27.3	11.3	32.0	10.5	17.2	1.8	-	26
<b>5</b>	38.0	6.1	18.0	12.8	22.9	-	2.2	29

In general, the slags are similar in the different trials, except for some exceptions. Namely, that the slags in trials 1 and 2 contain more than 54 mass-% FeO while the slag used in trial 3 contain 2.5 mass-% FeO. Also, all slags contained low amounts of MnO. This was important since it was used as tracer for the mixing time trials. It was only considered for the slag used in trial 5 when the amount of liquid phase was investigated for the Thermo-Calc calculations. This was due to that the slag contained more than 1 mass-% MnO.

The operating slag temperatures are somewhere around 1200 to 1600°C. For all Thermo-Calc calculations both a closed system and an open system with oxygen potentials that were in equilibrium with the surrounding atmosphere were considered. The oxygen potential was also varied for the different slags to be able to determine the variation in the melting temperature. The results from the calculations for the slags in trials 1 and 2 are shown in figures 25, 26 and 27. These results are selected since they contain the highest amounts of FeO. Therefore, they are most important due to that the composition is closest to the composition in slag in the future up-scaled IronArcs production process. These calculations were performed for an atmospheric pressure. In figure 25, the results for the closed system are shown. According to the results obtained from the closed system, the slag at 1000°C have a 30 % liquid phase content and is present in a liquid, completely melted, state at 1250°C. This is in line with the LOM investigation results that indicate that the slag is in a liquid state at the operating temperature.

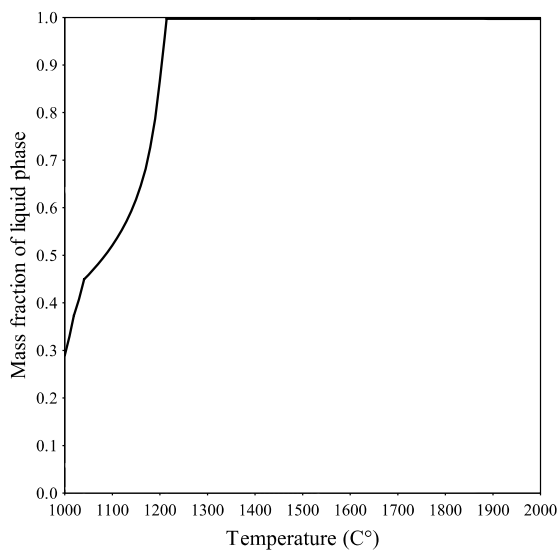


**Figure 25: The mass fraction of liquid phase for the slags used in trials 1 and 2 for a temperature span between 1000 and 2000 °C. The calculations were made for a closed system.**

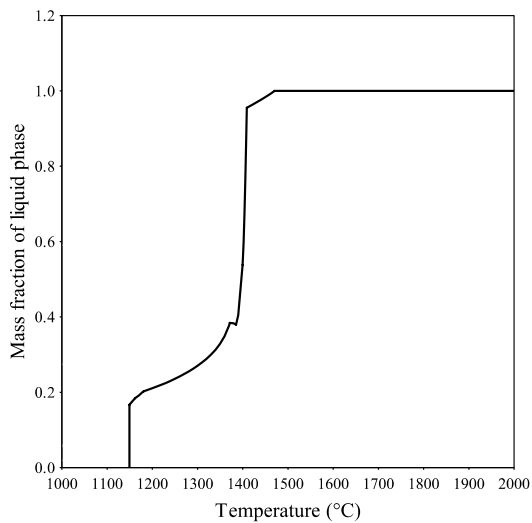


**Figure 26: The mass fraction of liquid phase in the slags used in trials 1 and 2 for a temperature span between 1000 and 2000 °C. The calculations were done by assuming an open system with an oxygen potential of 0.3.**

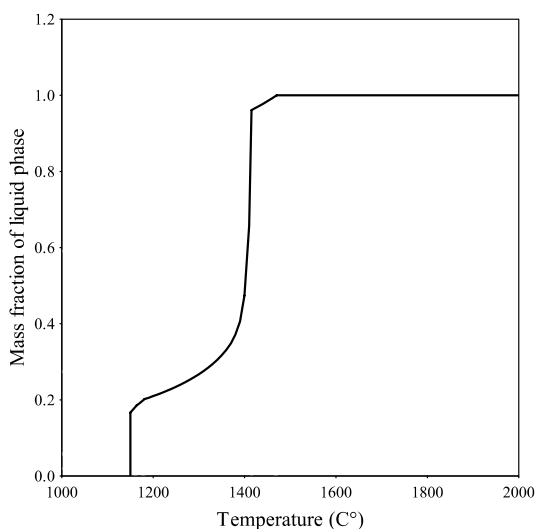


**Figure 27: The mass fraction of liquid phase in the slags used in trials 1 and 2 for a temperature span between 1000 and 2000 °C. The calculations were done by assuming an open system with an oxygen potential of 0.8.**

Figure 26 shows the mass fraction of the slag for an open system, where the slag is in equilibrium with an oxygen potential of 0.3. Figure 27 presents a similar calculation, but with an oxygen potential of 0.8. For both cases the melting starts at a higher temperature than given by the closed system. Furthermore, the slags have reached a liquid state which is higher than 90% at 1400°C and is fully liquid at approximately 1470°C. According to the predictions, the oxygen potential does not affect the melting temperature to a large extent. Specifically, the curves representing a liquid amount of 95 % differs by only 0.4%, when comparing the data for oxygen potentials values of 0.3 and 0.8 (figure 9 and 10). A completely liquid slag is reached at the same temperature. A larger difference exists between an open and closed system, where the melting temperatures are 1250°C and 1450°C according to the results for the slag compositions given in table 8. However, both the results obtained from an open and closed system indicate that the slag is in a liquid state during the operation of the pilot plant reactor. The results for the open system show a melting temperature that is closer to and on the limit of the pilot plant operation conditions. Similar calculations were done for trials 3 to 5, for a closed system as well as for both higher and lower oxygen potentials. The results for these calculations were similar, but the closed system was closer in melting temperature to the open system compared to the slag used in trials 1 and 2. Also, the melting temperature for these slags were predicted to be

approximately 1400°C. Another interesting factor is that the total number of elements in the slags are between 20 and 29. This is a lot higher than the number of elements that is used in the Thermo-Calc calculations. The melting point should not be higher than the predicted values due to the fact that a higher number of elements results in a lower melting point for some alloys compared to the pure metals of that alloy. It is shown that eutectic alloys systems often offer lower melting points than for the pure elements as well as still have a good fluidity [68]. Furthermore, some of the elements that were not included in the calculations were sodium oxides, potassium oxides and boron oxides. These elements work as fluxes. Therefore, it is likely that the melting temperature of the slag will be even lower than the predicted values using Thermo-Calc [69-70]. Also, previous investigations have shown that for a slag containing the main elements Fe, Si and O and accounted for 90 % of the slag has a main phase which is fayalite and that has a melting point of 1200°C [71]. This is similar to the slags in trial 1 and 2 which contains the main elements Fe, Si and O (combined amount of 90.6 mass-%). When combining the results from the LOM investigation, the mixing time experiments and also the Thermo-Calc calculations the slag in the pilot plant can be assumed to be in liquid state during operation.

### 3.1.2.1.3. WATER-AIR (SUPPLEMENT 5)

The results from the conductivity measurements in the pilot plant with water and air can be seen in Figure 28. This figure shows the conductivity values for probes 1 and 2. As soon as the sodium chloride tracer was added into the water, a rapid response in conductivity was found. The conductivity increased quickly for both probes and the final value was reached after seconds from the time of the tracer addition. According to these results, the mixing times are 8.5 seconds to reach a 95% degree of homogenization and 14 seconds to reach a 99% degree of homogenization. These results are in line with the other mixing time experiments that states that the bath is homogenized below 10 seconds for this process. This close agreement was obtained, even though the probes are positioned at another position etc.

The flow rate is 15% higher for the pilot plant experiment compared to the small-scale trials. The scaling flow rate was  $265 \text{ Nm}^3\text{h}^{-1}$  compared to the flow rate of  $230 \text{ Nm}^3\text{h}^{-1}$  used for this investigation. The mixing time was 10.6% faster for a 95% degree of homogenization in the pilot reactor compared to the small-scale reactor. Furthermore, the mixing time was 27% shorter for a 99% degree of homogenization for the pilot-scale compared to the small-scale reactor. According to this comparison, the 10% difference in mixing time for a 95% degree of homogenization is

closer to the 15% difference in flow rate than the 27% difference in mixing time for a 99% degree of homogenization.

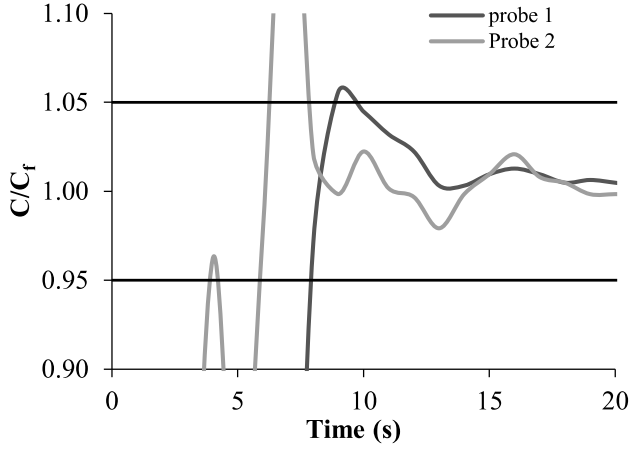


**Figure 28: Normalized conductivity values for the two measurement probes. Inside the horizontal lines at 1.05 and 0.95 represents the area where the concentration of the tracer is within a 95% degree of homogenization.**

## 3.2. NUMERICAL MODELING (SUPPLEMENTS 2 & 4)

### 3.2.1 PENETRATION DEPTH (SUPPLEMENT 2)

#### 3.2.1.1 VALIDATION CASE (EULER-EULER & VOF)

The penetration depth for a side blown small scale water model was determined by using two different numerical models; a Eulerian multiphase (EE) model and a VOF model. A mesh analysis was made for each model and the two model predictions were compared. The models had the same boundary conditions and the same meshes were used. The simulation time for predicting the penetration depth was 1.2 seconds. The penetration depth (or length) has been studied earlier by using numerical modeling. Both when using top blowing [16, 43, 44] and also a side blown gas injection [29, 41, 42, 46]. The VOF multiphase model has often been used for this purpose [29, 46, 18], while the Eulerian multiphase model has not been used to a large extent. There are cases where the Eulerian multiphase model has been used to determine the horizontal injected penetration depth. [42] Sometimes, the penetration depth is defined as the longest depth from the injecting nozzle where the gas volume fraction drops below 80 %. These results are valid regardless of the vertical position of the plume. [42, 47] For other cases, the penetration depth was defined

as the longest distance the injected gas reached along the centerline of the nozzle [24]. This definition was used for the simulations to determine the distance at the centerline of the nozzle measured from the nozzle wall to a distance where the volume fraction is 80%. If no nodes along the centerline for the different were positioned at that volume fraction, the distance was determined by using an interpolation. The gas plume in the water can be seen in Figure 29 and Figure 30 for the EE model and VOF model, respectively.

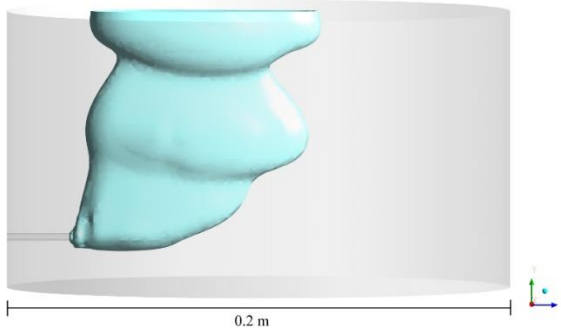


**Figure 29: Isosurface of the air plume in water for the EE-simulation.**

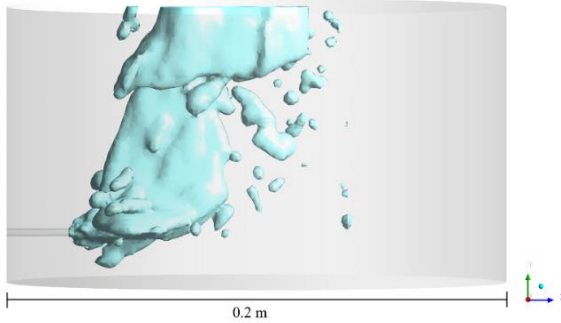


**Figure 30: Isosurface of air plume in the water for the VOF-simulation.**

In Figure 31 and Figure 32, the volume fraction of air as a function of the distance from the inlet along the center line of the nozzle is shown after 1.2 seconds for both models. In addition, contour plots are shown in Figure 33 and Figure 33. The fluctuations in the bath was tested for the coarse mesh

and showed that the penetration depth was approximately the same even after 20 seconds of blowing. Therefore, the flow in the tank had reached some sort of steady state value. Moreover, for a fixed point in the water the maximum fluctuation of the velocity was only a couple of mm/s. The EE model calculates both the gas and liquid. The sharpest interface between gas and liquid is shown for the fine mesh followed by the medium mesh and finally the coarse mesh. A maximum deviation of just below 3% is shown between the fine and medium meshes, while the deviation between the coarse and medium meshes is approximately 10%. The numerical diffusion is one contributing factor for the coarse mesh results, where the incline of the line shows that the air volume fraction is flatter compared to both the medium and fine meshes. This leads to a smearing of the gas water interface. The further away from the inlet the air reaches for the different meshes, the flatter the line inclination gets. A reason for this may be that the air travels both in the vertical and horizontal directions (due to momentum of the jet and the buoyancy of the bubbles). This gives the grid an inclined alignment to the air flow and in turn an increased amount of numerical diffusion. This phenomenon is well known [72]. With the experimental results and uncertainties, both the medium and fine meshes are deemed to be satisfactory good enough to be used to predict the gas penetration depth.

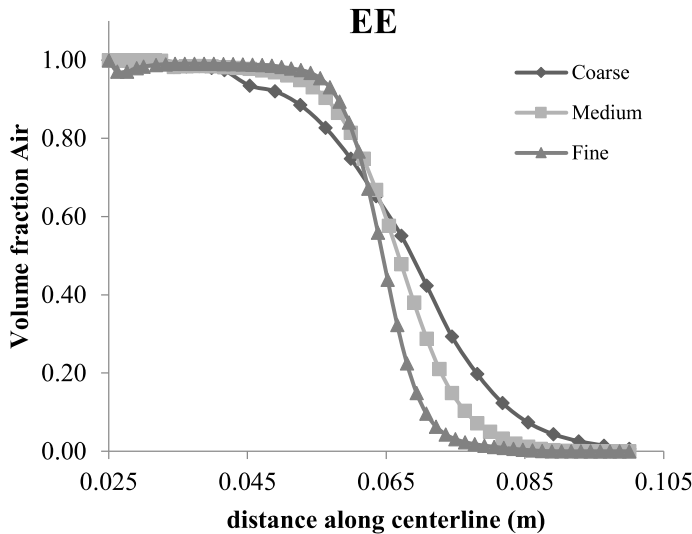


**Figure 31: Volume fraction of air as a function of distance along the nozzle centerline for EE-simulation.**



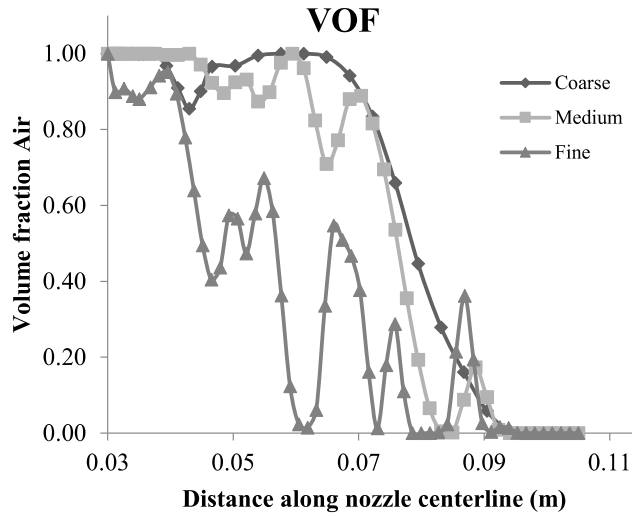


**Figure 32: Volume fraction of air as a function of distance along the nozzle centerline for VOF-simulation.**

For the VOF simulations, as can be seen in Figure 32 and Figure 34, the results are more scattered. Specifically, the volume fraction of the air does not follow the same trend as seen in the EE simulations. As the number of cells increases, the volume fraction value fluctuates more along the measured line. When the mesh gets finer, more bubbles are formed, and the plume shape gets more irregular. This can be seen in Figure 9, where the volume fractions for the gas plumes for all meshes are shown. The data shows different plume shapes and an increase in the amount of bubbles as the mesh is refined. Due to this formation of bubbles, large fluctuations in the air volume fraction appears. A definition of the penetration depth for an 80% volume fraction does not give a valid description of the penetration depth for the VOF predictions. The fine mesh would according to this be 3.7 centimeters, which is not the case. For this kind of bubbly plume maybe a plane gives a better representation than a line or a measurement over time, due to this irregular bubble movements. It should be noted that the VOF model is not a bad model to use to simulate the plume penetration, but it requires longer simulation times compared to the EE model.

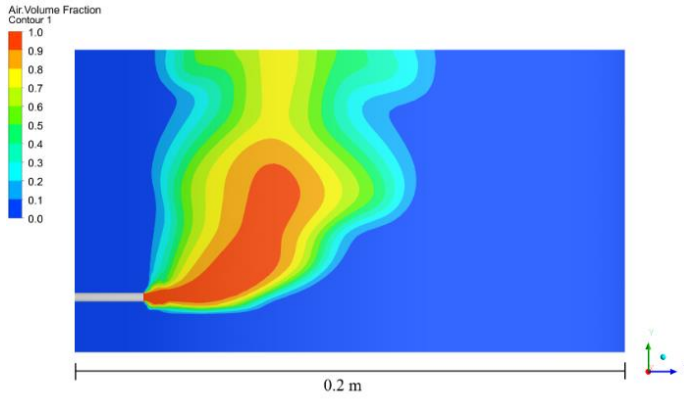


**Figure 33: Volume fraction of air when using the EE-model. Data are given for an yz-plane located in the center of the domain.**

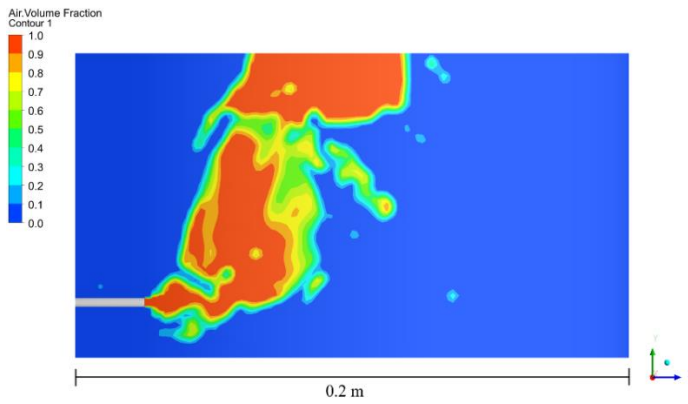


**Figure 34: Volume fraction of air when using the VOF-model. Data are given for an yz-plane located in the center of the domain.**

**Table 7: Penetration depths for the two multiphase models and for one experimental value.**

<b>Name</b>	<b>Multiphase model</b>	<b>Mesh</b>	<b>Number of cells</b>	<b>Penetration depth (m)</b>
<b>Mesh 1</b>	EE	Coarse	64000	0.058
	VOF	Coarse	64000	0.068
<b>Mesh 2</b>	EE	Medium	181000	0.060
	VOF	Medium	181000	0.067
<b>Mesh 3</b>	EE	Fine	350000	0.060
	VOF	Fine	350000	0.037
<b>Experimental</b>	-	-	-	0.070

In Table 7, the penetration depths for the VOF and EE simulations are compared for the different meshes. For the EE case, the medium mesh showed a penetration depth that was 99.8% of that of the fine mesh. Moreover, for the VOF simulation the penetration depth of the fine mesh is almost half the length compared to that of the medium mesh according to the current definition, due to an irregular shaped plume that contains more bubbles. The penetration depth of 6 cm for the EE simulation is close to the corresponding experimental penetration depth of 7 cm. Consequently, a small deviation between the penetration depth of the experimental value and the simulated value is expected.

Another thing that is to be considered is the simulation time. Here, the VOF simulations take longer times than the EE simulations, when the corresponding meshes are compared. A comparison of the simulation time for the coarse mesh showed that the simulation time of the EE simulation was 10% of that of the VOF simulation. These observations do not mean that the VOF model is an inaccurate model to use for the determination of the penetration depth during gas injection into a liquid. The Eulerian multiphase model has often been considered to be the multiphase model

that is the most complex of the existing multiphase models and that has a high computational expense [65]. This is because of the strong coupling between the phases and the available interaction terms (and due to that a set of equation is solved per phase), giving the possibility to include a lot of forces of the secondary phase. Due to that not all interaction parameters have been considered in this EE-simulation, the simulation time could be reduced. Compared to the VOF-simulations it was also possible to use a much larger time step in the EE simulation, namely  $1e-4$  instead of around  $5e-6$ .

### 3.2.1.2. PREDICTED PENETRATION DEPTH IRONARC (SUPPLEMENT 2)

The penetration depth of the IRONARC pilot plant was determined after validation of the PD model. Figure 35 shows the volume fraction of gas in the slag. The predicted penetration depth was estimated to be approximately 0.3 m, meaning that the gas travels half the distance of the diameter of the bottom cylinder of the reactor. The gas plume rises close to the nozzle wall, without being in contact with the wall. This is good since if the plume would rise at the wall, it would increase the wear of the freeze lining and would result in a higher energy consumption if an additional cooling would be needed. It will also result in a less effective energy usage, since some part of the gas will use its energy to heat the wall instead of the slag. The penetration depth should be long enough so that the gas bubbles are distributed throughout the slag bath and also so that the mixing is efficient, since mixing plays a major part in the process.

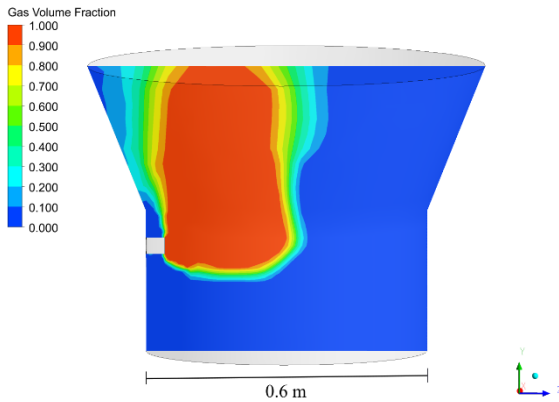


**Figure 35: Volume fraction of gas for the pilot scale-model in an yz-plane located in the center of the domain.**

Accurate modelling of the penetration depth is also very important for the future upscaling as well. The future reactor for the industrial process will be much larger, both with respect to the amount of charged slag as well as vessel dimensions. For the mixing properties in this pilot plant reactor the penetration depth is sufficient, due to that the gas is distributed well within the slag bath. However, it will be shorter compared to the diameter of the larger future reactor. This is because the upscaling is limited by the gas flow rate that can pass through an individual plasma generator. Therefore, more plasma generators will be used in an upscaled version instead of bigger ones. It was also shown that the initial penetration is longer than the depth after some time, when the injection of the gas has been somewhat stabilized. The fluctuations in penetration depths were also shown to be greater for the gas-slag system compared to the air-water system. An explanation may be the greater density difference between the gas and liquid in the gas-slag system compared to air-water. Overall, penetration depth predictions give no indications that discourage the upscaling of the reactor

### 3.2.2. MIXING TIME

#### 3.2.2.1 VALIDATION CASE (WATER MODEL)

The mixing time was predicted by using mathematical modeling and the numerical model results were compared to physical model results. This can be seen in figure 36, which shows the mixing time curves. Plotted as the tracer concentrations over time. Figures 36a) and b) show the curves for the numerical predictions and figures 36c) and d) the concentration curves from the water model experiment. For both the numerical and experimental results, the effect of the tracer is seen as an immediately increase in concentration at the measured point. Thereafter, the curves reach a peak value before being evened out at a unity value (1). However, the curves are slightly different in appearance. For the numerical results (Figure 36 a) the peak concentration is approximately 3.5 times the final value, while for the experimental case (Figure 36 c) the peak value only reaches just above 1.1. This difference in concentration curve appearance is due to the tracer addition in the different cases. For the water model experiments, the tracers were poured into the water. This convection causes the tracer content at the probe position to be more diluted compared to the numerical model simulations. Specifically, the tracer in the numerical model was patched into the domain as a spherical shape. Hence, a larger amount of tracer will take place at the probe location and in turn there will be a higher peak for the numerically predicted curves. For the physical water model experiments the average mixing times where 7.6 s and 10.2 s for a 95% and a 99% homogenization degree, respectively. This is true under the

condition that one inlet and a flow rate of 282 NLmin<sup>-1</sup> was used. The average predicted mixing time was found to be 7.5 seconds, which means that the difference between predicted and experimental mixing time was 1.3%. Moreover, the numerical model results are in good agreement with the physical model results in terms of predicting the mixing behavior.

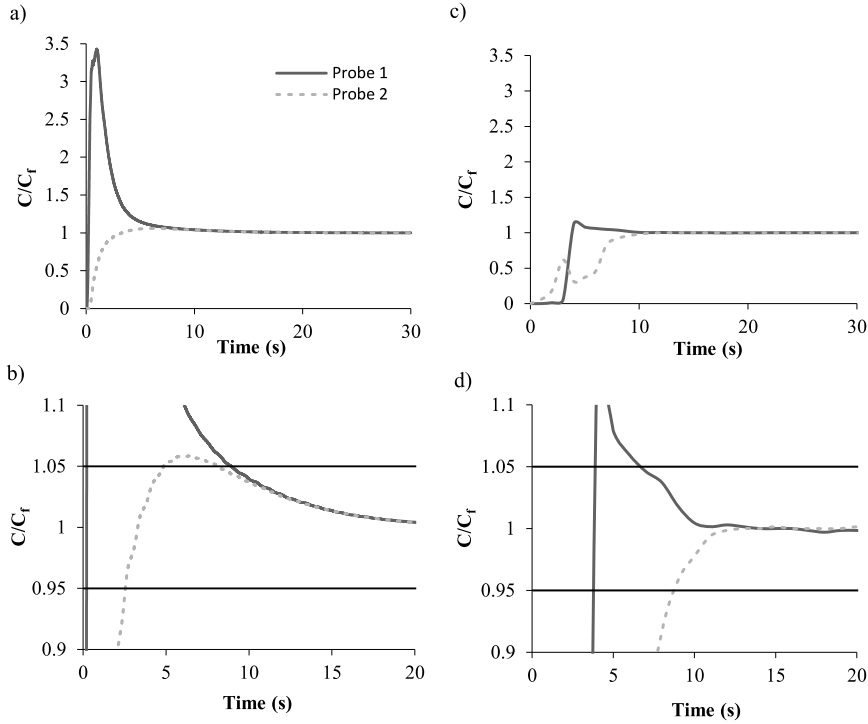


**Figure 36: Tracer concentration curves as a function of time for both predictions a) and b) and experiments c) and d)**

### 3.2.2.2 PREDICTED MIXING TIME IN IRONARC PILOT PLANT (SUPPLEMENT 4)

The numerical predicted mixing time in the pilot plant and the tracer concentration curves can be seen in Figure 37. These are similar to the results from the water model simulations in the sense that the point of measurement close to the addition position tracer increases to above two times the final concentration, while the other measurement point does not increase to the same level. However, both curves reach within the positions of the lines 1.05 and 0.95, which represents a 95% homogenization degree in the bath. This simulation predicted a mixing time of 6.5 seconds for a

95% homogenization degree. This is a mixing time that is below 10 seconds. Thus, these results are in line with the mixing time results from the earlier investigation, where the mixing times were determined in pilot plant trials. These results are in close agreement to the downscaled water model simulations results as well as the water model experiment results.

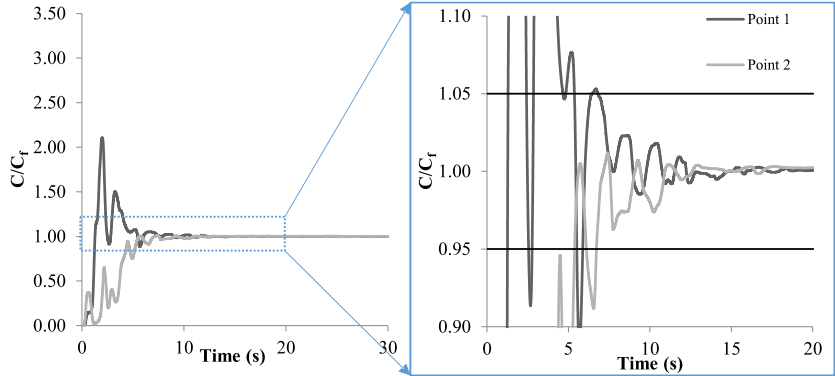


**Figure 37: Tracer concentration curves for the pilot plant slag simulation.**

The wall shear stress on the pilot plant reactor wall was predicted and the results are shown in figure 38a)-f). This figure shows the shear stress with a maximum of 30 Pa after 30 seconds of gas injection. The maximum shear stress value was found in the tuyere region and at the opposing wall of the tuyere. This area is located at the same height level as the tuyere and hence at the same level as the injected gas. The penetration depth of the gas injection in this process was determined to have a value of approximately 30 cm (center of reactor). Also, the opposing wall of the injected gas is affected by higher shear stresses even though the gas does not reach the wall. Moreover, the gas creates a flow, which will push the slag against that wall which will increase the shear stress. This is in line with the observed refractory wear during operation of this pilot plant process. Specifically, the wear has been found at approximately the same locations as these shear stress graphs shows.

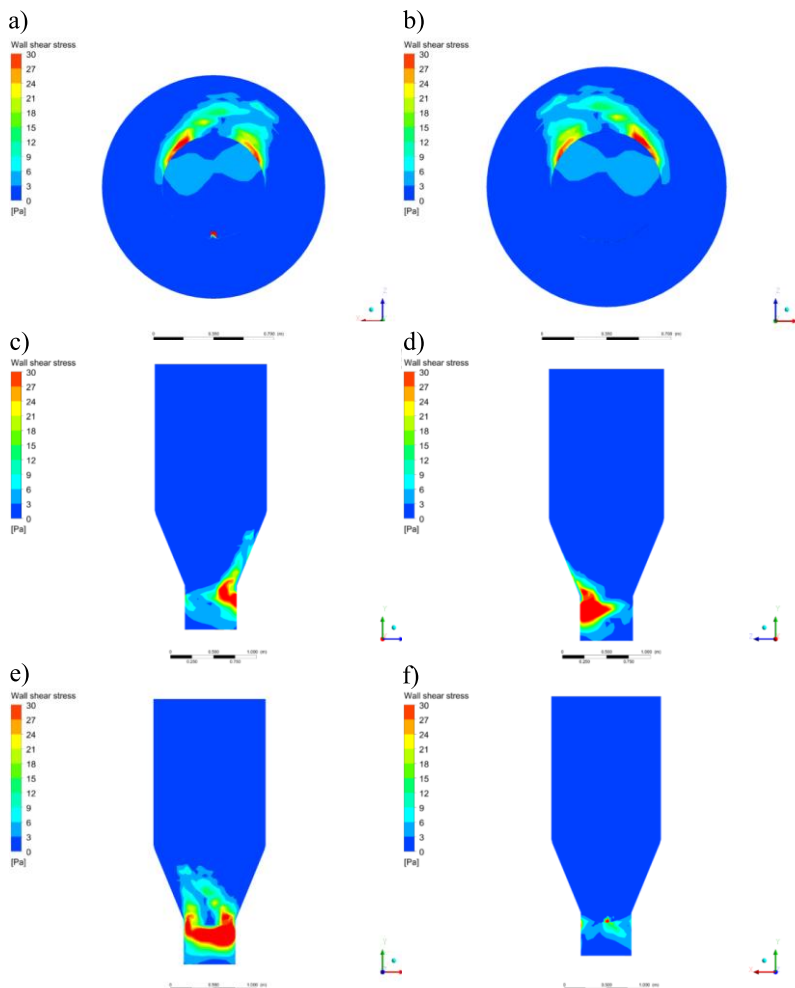


**Figure 38: The shear stress on the wall of the pilot plant with the maximum shear stress of 30 Pa. It is shown from a) above, b) below, c) right side, d) left side, e) opposite side of the nozzle locations, and f) nozzle wall.**



## 4. CONCLUDING DISCUSSION

---

This thesis focuses on investigating the fluid flow and mixing in the IronArc pilot plant process, both experimentally and numerically. This process is a new emerging technology for pig iron production to enable a more sustainable iron production compared to the existing blast furnace route. It uses submerged gas injection through plasma generators. In the process a hot and reducing carrier gas is injected into a slag consisting of iron oxides. The gas heats, creates stirring and also act as reducing agent in the process. Due to this, the stirring and mixing of this process is extremely important in order to have an efficient process for pig iron production. Also, the long-term goal (beyond this thesis) is to make an industrial process and therefore the information regarding the mixing and fluid flow is of great importance in a future upscaling of this IronArc technology. Moreover, the production rate of this process is dependent on the stirring, mixing time and penetration depth of the injected gas. This was investigated in this thesis that consists of 5 supplements that are listed in table 8. The table shows the objective, approach, parameters and the results of each supplement. A more detailed information regarding the results can be found in respective supplement.

In order to investigate the fluid flow, stirring and to determine the mixing time in the pilot plant experimentally and numerically a 1/3 scale (of the pilot plant) acrylic plastic model were designed. Both the mixing times and penetration depths were investigated under different conditions in **supplement 1**, due to their importance to the process. The mixing in the small-scale model is fast, with the average mixing times of 7.6 s and 10.2 s for a 95% and a 99% homogenization degree, when one inlet and a flow rate of 282 NLmin<sup>-1</sup> was used. This was 15 % and 18 % (per degree of homogenization) faster compared to the case when using 3 gas inlets and the same flow rate. A strong flow was created in the bath and it had a periodic movement that caused the water to circulate around the walls in the model for the one inlet case but was not seen to the same extent in the three-inlet case. The penetration depth was also investigated at different flow rates. Moreover, the maximum penetration depth at a flow rate slightly higher than the corresponding flow rate to the pilot plant was to slightly longer than the center of the reactor. These results are of big importance and also serves as validation results for numerical simulations. One of the most important parameters for gas injection into liquid baths is the penetration depth of the gas into the bath. This is due to that it strongly influences the flow structure and hence the stirring and plume behavior in metallurgical processes in general and the IronArc process in particular.

Due to the importance of the penetration depth in this process it was investigated numerically in **supplement 2**. First a model validation was made for a water model case. Moreover, an Eulerian and VOF approach were compared and then the penetration depth were determined in the pilot plant. The results showed that it was easier to measure the penetration depth with the Eulerian multiphase model. Also, the simulation time were greatly reduced due to that it was possible to use a fixed larger time step for the Eulerian case compared to the VOF approach. Furthermore, the penetration depth prediction of the pilot plant showed that the plume was detached from the nozzle wall and also does not penetrate further than to the center of the cylindrical reactor. This, in turn results in a better energy usage of the gas along with a small refractory wear.

In **supplement 3**, the mixing time were investigated by performing pilot plant trials. A tracer ( $\text{MnO}_2$  powder) were fed from the top of the reactor and the time for the tracer to be homogenized in the slag were taken. Also, investigations of the liquid phase in the slag during operation were made. The results show that it is possible to get an estimation of the mixing time by addition of tracer in the pilot plant process. Furthermore, that the mixing time is below 10 seconds according to the experimental results. These results agreed with the downscaled model. The results were also used as further validation for the numerical prediction of the mixing time in the pilot plant. Analysis of the slag indicated that the slag was in liquid state during operation. Both the LOM and Thermo-Calc investigation showed this tendency. This was important to be able to get correct properties of the slag during the numerical simulations. With this result the slag could be assumed to be in liquid state and also that it could be assumed to behave like a Newtonian fluid. Moreover, a reasonable value of the liquid viscosity could be determined.

With data from the downscaled water model experiments, the numerical simulations and data from the pilot plant trials a numerical model calculation of the mixing time were made in **supplement 4**. Firstly, the mixing time were predicted in the small-scale water model and the results were found to be in a good agreement with the physical model, with 1,3% difference when averaging the results for all the physical experiments. For specific trials the experimental results were within 20% of the predicted mixing time. Then, the mixing time were predicted for the pilot plant and resulted in a fast mixing of 6,5 seconds and thereby it agreed with both the downscaled model as well as the experimental trials that indicated that the mixing were below 10 seconds.

In **supplement 5** the opportunity was given to do mixing time experiments in the pilot plant, with water as liquid and a saline solution as a tracer. The same conductivity measurement approach was applied as in **supplement 1**. The goal with this investigation was to have further results to compare to the previous mixing time experimental results. Especially, as a comparison to the results in **supplement 3** that were made similarly but with hot slag as liquid medium. The overall results showed that the mixing times for 95% and 99% homogenization degrees were 8.5 s and 14 s, respectively. The mixing time of 8.5 seconds for a 95% degree of homogenization in the pilot-scale reactor was also in line with mixing time results reported earlier for trials performed with slag, as well as results for earlier small-scale physical model experiments.

**Table 8: overview of the supplements and the objective, approach, parameters and results**

	Study	Objective	Approach	Results
1	Physical Modeling Study on the Mixing in the New IronArc Process	Investigate and determine the mixing time and penetration depth. Obtain data for numerical simulations.	Down scaled physical water modeling. Conductivity measurements for mixing time. Video recordings, camera photos and high-speed camera used for penetration depth.	Mixing time determined to 7.6 s for a 95% homogenization degree for one inlet. Increased with 15.8% for the case when using 3 gas inlets.
2	Importance of the Penetration Depth and Mixing in the IRONARC Process	Compare suitable methods for determining penetration depth and validate the numerical model. Determine penetration depth in pilot plant.	Build up numerical model that corresponded to pilot plant. Compared VOF and Eulerian multiphase models in FLUENT for validation.	Eulerian multiphase model could accurately describe penetration depth (PD) with reduced simulation time. PD predicted in pilot plant to half of reactor.
3	Experimental Determinations of Mixing Times in the IronArc Pilot Plant Process	Determine the mixing time in the pilot plant experimentally. Determine slag phase during operation of process.	Addition of tracer in pilot plant and thereafter sampling during operation. LOM and Thermo-Calc investigation of the slag.	Possible to determine Mixing time by tracer addition (below 10 s) in pilot plant. Slag is in liquid state according to results from LOM and Thermo-Calc.
4	Numerical investigation of the mixing time in the IronArc Pilot Plant	Validate a numerical model for mixing time from water modeling. Simulate mixing time in Pilot plant process.	Numerical simulations of water model experiments as validation. Determine mixing time with validated model in pilot plant.	Mixing time was determined numerically by an Eulerian approach. The results agreed well with experimental results.
5	Physical modeling of the mixing in the IronArc pilot plant reactor	Investigate the mixing time in the pilot plant when filled with water, with known parameters. As comparison to mixing time measurements in previous supplements.	Pilot plant partially filled with water and saline solution added with conductivity measurements to determine the mixing time.	The mixing time was determined, and the results were in line with and reasonable when comparing to the other physical mixing time results.

## 5. CONCLUSIONS

---

In this study, the mixing times and penetration depths were investigated for the newly developed IronArc pilot plant process. This process is a new emerging technology for pig iron production and the idea of this technology is to become a sustainable alternative compared to the existing blast furnace route. It uses submerged gas injection through plasma generators. Both mixing times and penetration depths were investigated under different conditions. These parameters were the main focus due to their importance to the process and for a future up scaling, since this process is dependent on a fast mixing of the liquid slag bath. In **supplement 1** physical water model experiments were performed in a 1:3 scale acrylic plastic model of the IronArc pilot plant reactor. The mixing times was determined by measuring the conductivity in the water, after a sodium chloride solution was added to the bath. Furthermore, the penetration depth was investigated by using both a video camera and a high-speed camera. For **supplement 2** the penetration depth of the IronArc pilot plant process were investigated by mathematical modeling. Where first a model validation and a comparison between VOF and EE numerical models were made, followed by a simulation of the pilot plant. To get further knowledge about the mixing of the process the mixing time were investigated in pilot plant experimental trials for **Supplement 3**. In this supplement slag analysis were also made with both LOM investigation as well as with Thermo-Calc, which is useful information for both the understanding of the mixing phenomena, as well as for numerical calculations. With data and knowledge about slag, mixing times and penetration depths from previous supplements, the mixing times were determined by numerical calculations for the pilot plant in **supplement 4**. The opportunity was also given to perform water experiments in the pilot plant during a reconstruction of the reactor (**supplement 5**). For this supplement the mixing time were determined similarly as for the conductivity experiments in **supplement 1**. When summarizing the results of the supplements, following can be concluded:

- The mixing in the 1:3 scale model is fast, with the average mixing times of 7.6 s and 10.2 s for a 95% and a 99% homogenization degree. This was achieved when one inlet and a flow rate of 282 NLmin<sup>-1</sup> was used. Further results showed that an increased flow rate resulted in a reduced mixing time.
- When using three gas inlets, the average mixing times were 8.8 s and 12 s for 95% and 99% homogenization degrees, respectively.

This is an increase by 15.8% and a 17.6% of the mixing time for the 95% and 99% degrees of homogenizations, when multiple gas inlets were used compared to only using one gas inlet. A possible explanation was a periodic movement of the surface when using one gas inlet, which in turn, resulted in a circulation of the water along the walls in the model. Also, a calmer surface was seen when using three inlets with the same total flow rate.

- The penetration depth was measured and determined at several different flow rates and the results showed that an increased flow rate resulted in an increased penetration depth. The maximum penetration depth of the air for the flow rate of 300 NLmin<sup>-1</sup> was determined to have a value of 0.11 m. This means that the maximum penetration depth for the flow rate of 282 NLmin<sup>-1</sup> (a scaled flowrate corresponding to average flow rate of the pilot plant) will be slightly shorter. The penetration depth at the tuyere centerline showed a pulsating behavior, with a longer pulse followed by shorter ones. Furthermore, the length difference between the pulses increased with an increased flow rate. When the results were compared to an empiric equation from the literature, the results agreed better for low gas flow rates compared to high gas flow rates.
- The penetration depth of the experimental air water system could be described accurately by using both the EE (Euler-Euler) and VOF (Volume of Fluid) models. However, for the finest mesh of the VOF simulation, the fine-grained multiphase structure compared to the coarse and medium meshes made it more difficult to measure the penetration depth along the nozzle centerline. This was due to a more irregular plume and due to more bubble formation. A comparison showed that the EE simulation had a simulation time that was 10% of that of the VOF simulation, when comparing the coarse meshes. Due to that a longer time step could be used for the EE case.
- The penetration depth of the EE corresponded to the experiments within 86%. This is within the definition of an 80% volume fraction of gas along the nozzle centerline and describes the penetration depth for the EE simulation in an accurate way. This is a penetration depth that was very close to the reference physical experiment and gave a good description of the penetration of the air in the water.

- The penetration depth of the gas-slag system (IRONARC pilot plant) was calculated to have a value of approximately half the length of the reactor diameter (0.6m). This results in an efficient distribution of gas in the slag, which is important since it enhances the mixing and makes the bubbles reach large parts of the slag. This was in line with the results of the water modeling experiments.
- The overall results show that it was possible to approximately determine the mixing time by adding of a tracer ( $\text{MnO}_2$  powder) to the slag. The mixing time for the trials 3 to 5, with fast sampling, showed that the slag was homogenized just after a few seconds. More precisely for trial 3 the slag is likely homogenized after 8 seconds, but definitely after 16 seconds. The results from trial 4 and 5 showed the same tendencies, namely that the time mixing time, were reached already in the second samples, faster than 10 seconds after a tracer addition.
- It was seen in the LOM investigations that the microstructures were clearly dependent on the cooling speed. Where the finest structure was found in the area that had the fastest cooling speed and further into the sample where it had been cooled much slower, which resulted in a coarser structure. No particles that were not part of the solidification process could be seen. A phase prediction using the Thermo-Calc software, showed that a large majority of the slag or the entire slag was in a liquid state during the operating temperature. When combining these results, it is reasonable to conclude that the large majority of the slag was in a liquid state before it was cooled.
- The mixing time for the physical experiments were determined to be 7.6 seconds, based on the average mixing time for 6 trials performed to reach a 95% homogenization degree. This result is valid for one inlet and a flow rate of 282 NLmin<sup>-1</sup>. The mixing time for the numerical model was 7.5 seconds, which corresponds to a 1.3% difference compared to the experimental mixing times. Specifically, this means that the numerical model results are in good agreement with the physical model results in terms of predicting the mixing behavior.
- The predicted mixing time was 6.5 seconds in the hot pilot scale simulation, which is slightly faster than the water model mixing time. Specifically, the difference in mixing time is less than one

second. In addition, these results are in line with the mixing time results determined through industrial trials which showed that the mixing times were less than 10 seconds.

- The mixing times were determined for two different homogenization degrees in the water filled pilot plant. It was 8.5 seconds for a 95% degree of homogenization and 14 seconds for a 99% degree of homogenization. These results are in line with both numerical and experimental mixing time results obtained previous from this investigation. Namely that the mixing time in the IronArc pilot plant process are less than 10 seconds.



## 6. SUSTAINABILITY & FUTURE WORK

---

### 6.1 SUSTAINABILITY

This work contributes to the journey of making the steel industry a more sustainable industry, since it gives more knowledge and information about the novel IronArc process and is a step on the way in making it an industrial scale process. Also, this work has contributed in spreading information that this full scale industrial IronArc process will reduce the energy for producing iron compared to existing technologies. Also, since the material is melted in the first step, the process can charge a wide range of materials. Furthermore, it enables the use of renewable resources as the PG's operates on electricity compared to coke, which is used as input energy in the blast furnace. The energy efficiency in this future industrial scale process is based upon the fact that the CO gas in the reduction step is recirculated in the process and is used as reduction agent in the earlier step and as process gas in the plasma generators. Therefore, a future industrial process will contribute in reducing both energy consumptions and CO<sub>2</sub> emissions. Specifically, annual energy savings of 489 GWh based on an industrial process capacity of 500 000 tons per year. The total energy consumption amount per ton pig iron is 3100kWh, which is approximately 977kWh less than for the blast furnace. Also, a yearly decrease of 382 000 tons CO<sub>2</sub> and 160 000 tons of coke with the novel IronArc process compared to the blast furnace.[73] The results from this investigation contributes to fulfil the UN climate goals number 12 (responsible consumption and production) and 13(climate action). [74]

### 6.2 RECOMMENDATIONS OF FUTURE WORK

To be able to scale up the IronArc process and turn it into a commercial process there are several steps that needs to be made. Based on this investigation, some recommendations for the future work are listed below:

- Scale up the reactor and investigate the mixing in a larger scale reactor based on predictions of the mixing behavior using CFD.

- The future design plan now is to have two reactors, with a channel between these. The position of the channel should be investigated along with the material to be used in the slag channel. The channel needs to withstand and transport the FeO from the first reactor to the second reactor.
- The number and positions of PGs, the diameter of the larger scale reactor and bath depth should be investigated. These parameters are important when considering the design of a larger scale process.
- If the process should be operated continuously, it is also necessary to consider when determining how the larger scale process is designed.

## 7. REFERENCES

---

- [1] H. Sandberg, R. Lagneborg, B. Lindblad, H. Axelsson and L. Bentell, "CO<sub>2</sub> emissions of the swedish steel industry", *Scandinavian Journal of Metallurgy*, vol. 30, 2001, pp. 420-425.
- [2] D. Gielen, CO<sub>2</sub> removal in the iron and steel industry *Energy Conversion and Management*, 44, 2003 , pp. 1027-1037.
- [3] European Comission, SETIS, *Energy Efficiency and CO<sub>2</sub> reduction in the Iron and Steel Industry*, 2014.
- [4] World Steel Association, Worldsteel position paper, *Steels contribution to a low carbon future and climate resilient Societies*, 2017.
- [5] J. C. M. Farla, C. A. Hendricks and K. Blok: "Carbon dioxide recovery from industrial processes", *Climate Change*, 29, 1995, pp. 439-461.
- [6] K. Wang, C. Wang, X. Lu and J. Chen, "Scenario analysis on CO<sub>2</sub> emissions reduction potential in China's iron and steel industry", *Energy Policy* vol. 35, 2007, pp. 2320-2335.
- [7] D. Gielen and Y. Moriguchi, "CO<sub>2</sub> in the iron and steel industry: an analysis of Japanese emission reduction potentials", *Energy Policy*, vol. 30, 2002, pp. 849-863.
- [8] Y. Hashimoto, Y. Okamoto, T. Kaise, Y. Sawa and M. Kano, "Practical Operation Guidance on Thermal Control of Blast Furnace", *ISIJ International*, vol. 59, 2019, pp. 1573-1581.
- [9] L. Gan and H. Zhang, "Dangerous emissions in Blast Furnace Operations", *Springer International. Publishing*, Switzerland, 2016, pp. 125-137
- [10] H. Ahmed, "Recent trends in Ironmaking Blast Furnace Technology to Mitigate CO<sub>2</sub> Emissions: Top Charging Materials", *Springer International Publishing*, Switzerland, 2016, pp. 101-123
- [11] M. Santen and M. Imris: Patent SE 536 291, Issued august 6(2013)
- [12] M. Zhu, I. Sawada and M. Iguchi, "Physical Characteristics of a Horizontally Injected Gas Jet and Turbulent Flow in Metallurgical Vessels," *ISIJ International*, vol. 38, 1998, pp. 411-420.
- [13] M. Iguchi, Bubble and liquid flow characteristics during horizontal cold gas injection into a water bath, steel research, vol. 71, no. 11, 2000, pp 435-441.

- [14] A. Tilliander, L. T. I. Jonsson and P. G. Jönsson; "A three dimensional Three-Phase Model of Gas Injection in AOD Converters", *Steel Research International*, vol. 85, 2014, pp. 376-387.
- [15] D. Mazumdar, R. I. L. Guthrie: "Hydrodynamic Modeling of some Gas Injection Procedures in Ladle Metallurgy Operations", *Metallurgical transactions B*, vol. 16B, 1985, pp 83-90.
- [16] X. Zhou, M. Ersson, L. Zhong, J. Yu, P. G. Jönsson: "Mathematical and Physical Simulation of a Top Blown Converter", *Steel Research International*, vol. 85, 2014, pp. 273-281.
- [17] X. Zhou, M. Ersson, L. Zhong, J. Yu, P. G. Jönsson: "Optimization of Combined Blown Converter Process", *ISIJ International*, vol. 54. 2014, pp. 2255-2262.
- [18] X. Zhou, M. Ersson, L. Zhong, P. G. Jönsson: "Numerical and Physical Simulations of a Combined Top-Bottom-Side Blown Converter", *Steel Research International*, vol. 86, 2015, pp. 1328-1338.
- [19] V. Visuri, E. Isohookana, A. Kärnä, T. Haas, R.H. Eriç, T. Fabritius, 5th International Conference on Process Development in Iron and Steelmaking, Luleå Sweden, June 2016.
- [20] C. Wupperman, N. Giesselmann, A. Rückert, H. Pfeifer, H. Odenthal: "A Novel Approach to determine the Mixing in a Water Model of an AOD Converter", *ISIJ International*, vol.52, 2012, pp. 1817-1823.
- [21] P. Samuelsson, P. Ternstedt, A. Tilliander, A. Apell, P. G. Jönsson: "Use of physical modelling to study how to increase the production capacity by implementing a novel oblong AOD converter", *Ironmaking & Steelmaking*, vol. 45, 2018, pp. 335-341.
- [22] P. Ternstedt, A. Tilliander, P. G. Jönsson, M. Iguchi: "Mixing time in a side-blown converter", *ISIJ international*, vol. 50, 2010, pp. 663-667.
- [23] A. Tilliander, T. L. I. Jonsson, P. G. Jönsson: "Fundamental Mathematical Modeling of Gas Injection in AOD Converters", *ISIJ International*, vol. 44, 2004, pp. 326-333.
- [24] M. Bjurström, A. Tilliander, M. Iguchi, P. G. Jönsson: "Physical-modeling Study of Fluid Flow and Gas Penetration in a Side-Blown AOD Converter", *ISIJ International*, vol. 46, 2006, pp. 523-529.
- [25] J. H. Wei, J. C. Ma, Y. Y. Fan, N. W. Yu, S. L. Yang, S. H. Xiang, D. P. Zhu: "Water modelling study of fluid flow and mixing characteristics in bath during AOD process", *Ironmaking & Steelmaking*, vol. 26, 1999, pp. 363-370.

- [26] J. H. Wei, H. L. Zhu, Q. Y. Jiang, G. M. Shi, H. B. Chi, H. J. Wang: "Back-attack Phenomena of Gas Jets with Submerged Horizontally Blowing and Effects on Erosion and Wear of Refractory Lining", *ISIJ International*, vol. 39, 1999, pp. 779-786.
- [27] J. H. Wei, N.-W. Yu, Y.-Y. Fan, S.-L. Yang, J.-C. Ma and D.-P. Zhu: "Study on flow and mixing characteristics of molten steel in RH and RH-KTB refining processes", *Journal of Shanghai University*, vol. 6 2002, pp. 167-175.
- [28] T. M. J. Fabritius, P. T. Mure and J.J Härkki: "The Determination of the Minimum and Operational Gas Flow Rates for Sidewall Blowing in the AOD-Converter", *ISIJ International*, vol. 43, 2003, pp. 1177-1184.
- [29] H. J. Odenthal, U. Thiedemann, U. Falkenreck and J. Schlueter: "Simulation of Fluid Flow and Oscillation of the Argon Oxygen Decarburization (AOD) Process", *Metallurgical and Materials Transactions B*, vol. 41, 2010, pp. 396-414.
- [30] T. M. J. Fabritius, P. A. Kupari and J. J. Harkki: "Physical modelling of a sideall-blowing converter", *Scandinavian Journal of Metallurgy*, vol. 30, 2001, pp. 57-64.
- [31] C. Wupperman, A. Rückert, H. Pfeifer and H. Odenthal: "Physical and Mathematical Modeling of the Vessel Oscillation in the AOD process", *ISIJ international*, vol. 53, **2013**, pp. 441-449.
- [32] J. H. Wei, H. L. Zhu, H. B. Chi and H. J. Wang: "Physical Modeling Study on Combined Side and Top Blowing AOD Refining Process of Stainless Steel: Fluid Mixing Characteristics in Bath", *ISIJ International*, vol. 50, 2010, pp. 26-34.
- [33] R. I. L. Guthrie, M. Isac and Z. H. Lin: "Fluid dynamics simulation of chromium recovery from AOD slags during reduction with ferrosilicon additions", *Ironmaking & Steelmaking*, vol. 32, 2005, pp. 133-140.
- [34] E. O. Hoefele and J. K. Brimacombe: "Flow Regimes in Submerged Gas Injection", *Metallurgical Transactions B*, vol. 10B, 1979, pp. 631-648.
- [35] M. P. Schwarz: "Simulation of gas injection into liquid melts," *Applied Mathematical Modelling*, vol. 20, 1996, pp. 41-51.
- [36] M. Bjurström, A. Tilliander, M. Iguchi and P. Jönsson: "Physical-modeling Study of Fluid Flow and Gas Penetration in a Side-blown AOD Converter," *ISIJ International*, vol. 46, 2006, pp. 523-529.
- [37] M. Zhu, I. Sawada and M. Iguchi, "Physical Characteristics of a Horizontally Injected Gas Jet and Turbulent Flow in Metallurgical Vessels," *ISIJ International*, vol. 38, 1998, pp. 411-420.

- [38] G. N. Oryall and J. K. Brimacombe: "The Physical Behaviour of a Gas Jet Injected Horizontally into Liquid Metal," *Metallurgical Transactions B*, vol. 7B, 1976, pp. 391-403.
- [39] R. Hurman Eric: "Physical Modeling Study of Ferroalloy/Stainless Steel Refining Reactors", *Materials and Manufacturing Processes*, vol. 23, 2008, pp. 769-776.
- [40] N. Kochi, K. Mori, Y. Sasaki and M. Iguchi: "Mixing Time in a Bath in the Presence of Swirl Motion Induced by Horizontal Gas Injection with an L-Shaped Lance", *ISIJ international*, vol.51, 2011, pp. 344-349.
- [41] J.-N. Tang, C. Tseng, N. Wang and W. Shyy: 49th AIAA Aerospace Science Meeting including the New Horizons Forum and Aerospace Exposition, Florida, 2011.
- [42] N. Huda, J. Nazer, G. Brooks, M. A. Reuter and R. W. Matuszewicz: "Computational fluid dynamics (CFD) investigation of submerged combustion behavior in a tuyere blown slag-fuming furnace", *Metallurgical and Materials Transactions B*, vol. 43B, 2012, pp. 1054-1068.
- [43] M.K. Mondal and K. Logachander: *IJRET: International Journal of Research in Engineering and Technology*, vol 02, 2013, pp. 451.
- [44] H. Odenthal, U. Falkenreck and J. Schlüter: "CFD Simulation of Multiphase Melt Flows in Steelmaking Converters", *European Conference on Computational Fluid Dynamics (ECCOMAS CFD)*, 2006.
- [45] Z. Hongliang, L. Tingting, Y. Pan, M. Liangzhaoi and L. Fengqin; "An Experimental and Simulated Study on Gas-Liquid Flow and Mixing Behaviour in an ISASMELT Furnace", *Metals*, vol. 9, 2019, pp. 565-578.
- [46] A.Valencia, M. Rosales, R. Paredes, C. Leon and A. Moyano: "Numerical and experimental investigation of the fluid dynamics in a Teniente type copper converter", *International Communications on Heat and Mass Transfer*, vol. 33, 2006, pp. 302-310.
- [47] R. Hong, H. Li, H.Li and Y. Wang: "Studies on the inclined jet penetration length in a gas-solid fluidized bed", *Powder Technology*, vol. 92, 1997, pp. 205-212.
- [48] Y. Li, W. T. Lou, M. Y. Zhu: "Numerical simulation of gas and liquid flow in steelmaking converter with top and bottom combined blowing", *Ironmaking & Steelmaking*, vol.40, 2013, 40, pp. 505-514.
- [59] D.K. Chibwe, G. Akdogan, C. Aldrich and R. H. Eric: "CFD Modelling of Global Mixing Parameters in a Pierce Smith Converter with Comparison to

Physical Modelling”, *Chemical product and process modeling*, vol. 6, 2011, pp. 1-28

[50] Q. Zhang, Y. Yong, Z.-S. Mao, C. Yang and C. Zhao: “Experimental determination and numerical simulation of mixing time in a gas stirred-liquid stirred tank”, *Chemical Engineering Science*, vol. 64, 2009, pp. 2926-2933.

[51] M. Jahoda, L. Tomaskova and M. Mostek: “CFD Prediction of liquid homogenization in gas-sstirred tank, *Chemical Research and Design*”, vol. 87, 2009, pp. 460-467.

[52] M. Madan, D. Satish and D. Mazumdar: “Modeling of Mixing in Ladles Fitted with Dual Plug, *ISIJ International*”, vol. 45, 2005, pp. 677-685.

[53] F. D. Maldonado-Parra, M. A. Ramirez-Argaez, A. N. Conejo and C. Gonzalez: “Effect of Both Radial Position and Number of Porous Plugs on Chemical and Thermal Mixing in an Industrial Ladle Involving Two phase flow”, *ISIJ International*, vol. 51, 2011, pp. 1110-1118.

[54] A. Valencia, M. Rosales-Vera and C. Orellana: “Fluid Dynamics in a Teniente Type Copper Converter Model with One and Two Tuyeres”, *Advances in Mechanical Engineering*, vol. 2013, pp. 1-8.

[55] E. K. Ramasetti, V.-V. Visuri, P. Sulasalmi, T. Fabritius, T. Saatio, M. Li and L. Shao: Numerical Modeling of Open-Eye Formation and Mixing Time in Argon Stirred Industrial Ladle, *Metals*, vol. 9, 2019, pp. 1-12.

[56] M. K. Mondal, N. Maruoka, S. Kitamura, G. S. Gupta, H. Nogami and H. Shibata: “Study of Fluid flow and Mixing Behaviour of a Vacuum degasser”, *Transactions of the Indian Institute of Metals*, vol. 65, 2012, pp. 321-331.

[57] H. Ma, X. Chen, H. Hwang, M. Pratt, R. J. Mulligan, B. Wu, G. Tang and C. Q. Zhou: “CFD Modeling of a Ladle with Top Stirring Lance”, *CFD Modeling and Simulation in Materials Processing*, 2016, pp. 167-177.

[58] H. Kasban, O. Zahran, H. Arafa, M. El-Kordy, S.M.S Elaraby, F.E. Abd. “Laboratory experiments and modeling for industrial radiotracer applications”, *Applied Radiation and Isotopes*, vol. 68, 2010, pp. 1049-56.

[59] N. Othman and S. K. Kamarudin: “Radiotracer Technology in Mixing Processes for Industrial Applications”. *The Scientific World Journal*, vol. 2014, 2014, pp. 1-15.

[60] D. L. Perry: *Handbook of inorganic compounds*, 2<sup>nd</sup> ed. CRC press, 2011, pp. 267-268.

- [61] Y. Fujii, Y. Nakai, Y. Uchida, Y. Miki. Fundamental investigation of high temperature reduction and melting behavior of manganese ore. *ISIJ international*, vol. 57, 2017, pp. 609-614.
- [62] J.O. Andersson, T. Helander, L. Höglund, P. Shi, and B. Sundman: “Thermo-Calc & DICTRA, computational tools for materials science”, *Calphad*, vol. 26, 2002, pp. 273-312.
- [63] TCOX7, *TCS Metal Oxide Solutions Database*, Version 7, Thermo-Calc Software AB
- [64] K. Bölke, M. Ersson, P. Ni, M. Swartling and P.G. Jönsson: “Physical Modeling Study on the Mixing in the New IronArc Process”, *Steel Research International*, vol. 89, 2018, pp. 1-10.
- [65] ANSYS 15.0 Fluent Theory Guide, ANSYS Inc., USA, 2013.
- [66] F. Kerdouss, A. Bannari and P. Proulx: “CFD modeling of Gas Dispersion and Bubble Size in a Double Turbine Stirred Tank”, *Chemical Engineering Science*, vol. 61, 2006, pp. 3313-3322.
- [67] P. Chen, J. Sanyal and M.P. Dudukovic: “CFD modeling of bubble columns flows: implementation of population balance”, *Chemical Engineering Science*, vol. 59, 2004, pp. 5201-5207.
- [68] C. Morando, O. Fornaro, O. Garbellini and H. Palacio. Fluidity on Metallic Eutectic Alloys. *Procedia Materials Science*, vol. 8, 2015, pp. 959-967.
- [69] M. Hasanuzzaman, A. Rafferty, M. Sajja and A.-G. Olabi: “Production and Treatment of Porous Glass Materials for Advanced Usage”, *Reference Module in Materials Science and Materials Engineering*, 2016, pp. 1-11.
- [70] J. Britt: *The Complete Guide to High-Fire Glazes*, Sterling Publishing Co., inc. New York, USA, 2004, pp. 18-19.
- [71] X. Cheng, k. Zhao, Y. Qi, X. Shi and C. Zhen: “Direct Reduction Experiment on Iron-Bearing Waste Slag”, *Journal of Iron and Steel Research International*, vol. 20, 2013, pp. 24-29
- [72] B. Andersson, R. Andersson, L. Håkansson, M. Mårtenssen, R. Sudiyo, B. van Wachem and L. Hellström: “Computational Fluid Dynamics for Engineers”, *Cambridge University Press*, Cambridge, 2012.
- [73] Personal communication, M. Swartling, ScanArc Plasma technologies AB, Jan. 2020.
- [74] United Nations, 2020, *Sustainable development: UN's 17 sustainable development goals*, [<https://www.un.org/sustainabledevelopment/>].